Local Environments of Dilute Activator Ions in the Solid-State Lighting Phosphor Y$_{3−x}$Ce$_x$Al$_5$O$_{12}$

Nathan C. George,[†,▽] Andrew J. Pell,[‡] Géraldine Dantelle,[§] Katharine Page,[‖] Anna Llobet,[‖] M. Balasubramanian,[⊥] Guido Pintacuda,[‡] Bradley F. Chmelka,*[,†] and Ram Seshadri*[,#,▽]

[†]Department of Chemical Engineering, University of California, Santa Barbara, California 93106, United States

[‡]Centre de RMN à Très Hauts Champs, Université de Lyon/UMR 5280 CNRS/Ecole Normale Supérieure de Lyon/Université Claude Bernard Lyon 1, 5 rue de la Doua, 69100 Villeurbanne, France

[§]Laboratoire de Physique de la Matière Condensée, École Polytechnique, UMR 7643 CNRS, F-91128 Palaiseau, France

[‖]Lujan Neutron Scattering Center, Los Alamos National Laboratory, New Mexico 87545, United States

[⊥]X-ray Science Division, Advanced Photon Source, Argonne National Laboratory, Argonne, Illinois 60439, United States

[#]Materials Department and Materials Research Laboratory, University of California, Santa Barbara, California 93106, United States

[▽]Mitsubishi Chemical Center for Advanced Materials, University of California, Santa Barbara, California, 93106, United States

S *Supporting Information*

ABSTRACT: The oxide garnet Y$_3$Al$_5$O$_{12}$ (YAG), when substituted with a few percent of the activator ion Ce^{3+} to replace Y^{3+}, is a luminescent material that is nearly ideal for phosphor-converted solid-state white lighting. The local environments of the small number of substituted Ce^{3+} ions are known to critically influence the optical properties of the phosphor. Using a combination of powerful experimental methods, the nature of these local environments is determined and is correlated with the macroscopic luminescent properties of Ce-substituted YAG. The rigidity of the garnet structure is established and is shown to play a key role in the high quantum yield and in the resistance toward thermal quenching of luminescence. Local structural probes reveal compression of the Ce^{3+} local environments by the rigid YAG structure, which gives rise to the unusually large crystal-field splitting, and hence yellow emission. Effective design rules for finding new phosphor materials inferred from the results establish that efficient phosphors require rigid, highly three-dimensionally connected host structures with simple compositions that manifest a low number of phonon modes, and low activator ion concentrations to avoid quenching.

KEYWORDS: *inorganic phosphors, white solid-state lighting, structure–property relations, electron and nuclear magnetic resonance, X-ray and neutron scattering, X-ray absorption*
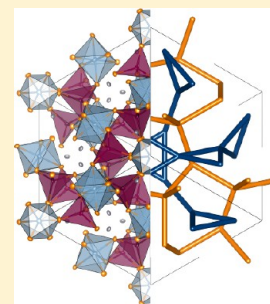
INTRODUCTION

While many strategies have been proposed for more efficient general lighting, including polymer[1] and small-molecule organic[2] and inorganic light-emitting diodes (LEDs),[3,4] down-conversion strategies based on inorganic light sources and phosphor conversion[5,6] have become the most widespread. Phosphor converted inorganic light-emitting diodes possess many advantages, including durability, long life, color stability, and a relatively benign environmental footprint, specifically in their being free of toxic heavy metals.[4,7] The oxide garnet Y$_3$Al$_5$O$_{12}$ (YAG), when substituted with a few percent of the activator ion Ce^{3+}, is a luminescent material that has nearly ideal photoluminescence properties for excitation by a blue solid-state light source. As a result, Y$_{3−x}$Ce$_x$Al$_5$O$_{12}$ continues to be the canonical phosphor with widespread use in solid-state lighting. Nevertheless, there is still limited understanding of how optical properties of doped YAG and other solid-state phosphors depend on the local structures and distributions of activator ions (usually Ce^{3+} or Eu^{2+}). The composition-structure–property relationships of Y$_{3−x}$Ce$_x$Al$_5$O$_{12}$ are central

to those of solid-state phosphors generally, and an understanding of such relationships is expected to provide insights on other phosphors such as silicates,[8] nitrides,[9−11] and oxy-nitrides,[12,13] to name a few. Moreover, similar issues concerning the local structures near dilute substituent ions are central to the properties of related solid-state oxides/compounds used as thermoelectrics,[14] ionic conductors,[15,16] luminescent upconversion materials,[17] quantum cutting phosphors,[18] battery electrodes,[19] structural cements,[20] photovoltaic materials,[21] and heterogeneous catalysts.[22,23]

Y$_{3−x}$Ce$_x$Al$_5$O$_{12}$ (henceforth YAG:Ce) was first studied and proposed for use in displays by Blasse and Bril in 1967.[24] When bright-blue InGaN diode light sources first became available,[25] YAG:Ce was quickly employed for the generation of white light *via* the partial down-conversion of the blue light from the solid-state device due to the nearly ideal optical characteristics of

YAG:Ce. These characteristics include a high refractive index, high quantum efficiency, substantial resistance to thermal quenching of the luminescence, appropriate matching of its excitation spectrum to emission from blue InGaN sources, and yellow emission in the complementary color region to the blue. The efficiently emitted green-yellow light from YAG:Ce mixes with the incident blue from the LED resulting in white emission; the phosphor particles also provide an effective light-scattering medium for the mixing.

Although YAG:Ce has been the subject of many studies and has seen widespread use, the crystal-chemical reasons for the nearly ideal optical properties of YAG:Ce have yet to be elucidated. Specifically, effective design rules for new and efficient phosphors based on the crystal chemistry of YAG:Ce would be tremendously valuable, though these currently do not exist. YAG:Ce is not a typical Ce-substituted oxide phosphor; whereas most Ce-substituted oxides emit in the blue or blue-green region,[26] YAG:Ce efficiently emits in the green-yellow region. It unusually combines the properties of a large crystal-field splitting, usually associated with polarizable ligands such as N^{3-} or S^{2-}, and a large band gap, usually associated with oxides and fluorides, which are difficult to reconcile. The large crystal-field splitting results in optical absorption of YAG:Ce peaking at around 460 nm and emission which peaks around 540 nm. These occur due to electronic transitions within Ce^{3+} between the $[Xe]4f^1 5d^0 6s^0$ ($^2F_{5/2}$, $^2F_{7/2}$) and $[Xe]4f^0 5d^1 6s^0$ ($^2D_{3/2}$) states.[24] The energy gap between these two states is significantly decreased from what is known for an isolated Ce^{3+} ion due to the large crystal-field splitting of Ce^{3+} 5d states, which arises when a Ce^{3+} ion replaces a smaller Y^{3+} ion in the YAG structure.[26,27] The crystal-field splitting of Ce^{3+} in YAG was found to be 2.22 eV,[28] which is unusually large for an oxide phosphor.[26] In addition to the unusual red-shifted emission of Ce^{3+} in YAG, YAG:Ce is known to be extremely bright, with quantum efficiencies at room temperature exceeding 85%.[29] The intrinsic quenching temperature of YAG:Ce deduced from decay time measurements was reported to be above 600 K for low Ce concentrations (<1 wt %) and above 400 K for higher Ce concentrations (>1%).[30] More recently, Setlur and Srivastava[31] examined the optical characteristics of YAG:Ce, finding that lower-energy Ce^{3+} sites become more numerous at relatively high Ce concentrations of around $x = 0.09$ in $Y_{3-x}Ce_xAl_5O_{12}$. The lower-energy Ce sites lead to a red-shift in emission and are thought to be due to either neighboring Ce–Ce ions and/or Ce in perturbed lattice sites, though the nature of these sites has remained unknown.

Though there have been several studies related to structure–property relationships in YAG:Ce and related compounds, most have sought to correlate emission color to the local or long-range structures of phosphors. To date, no studies suggest crystal-chemical guidelines for finding new and efficient phosphor compounds. Among the long-range structural studies, Robertson et al. reported emission spectra of epitaxially grown YAG:Ce films with various cation substitutions.[32] It was noted from this study that another effect besides cation size was responsible for color shifts of the emission spectra. This effect was investigated by Wu et al.[33] by correlating excitation and emission wavelengths to the average structural distortion of the active site in garnets. Pan et al.[34] have correlated the red-shift of emission to long-range crystalline structure in Gd^{3+}-substituted YAG:Ce, showing a strong dependence of the emission wavelength on the lattice parameter and strength of the crystal-field splitting of Ce^{3+}. One local structure study by

Furman et al. demonstrated that the quantum efficiency of bulk YAG:Ce and YAG:Ce nanoparticles was related to the degrees of crystallinity found from synchrotron X-ray total scattering.[35] Another recent study examined the local structure of the Ce^{3+} ion using Ce K-edge extended X-ray absorption fine structure (EXAFS) and found that the nearest eight Ce–O distances are expanded by about 3% compared to the average Y–O distances in $Y_{2.97}Ce_{0.03}Al_5O_{12}$.[36] Using first principles theory methods, Gracia et al.[37] and Munõz-García and Seijo[38] have suggested that substitution of Ce^{3+} for Y^{3+} in YAG:Ce results in a small expansion of the coordination environment around the substituent ion.

In light of the great importance of YAG:Ce and the challenges associated with the analysis of dilute substituent species in crystalline materials, we have employed a suite of powerful state-of-the-art structural probes, focusing on the local structure of Ce ions and their interactions with the YAG host lattice. The scattering and spectroscopic techniques used yield important new insights regarding the optical properties of YAG:Ce. More generally, these techniques enable precise structural analyses of substituent ions at small concentrations of approximately 1 mol %. Such analysis is useful not only when investigating phosphor materials but also potentially to other important materials with small doping amounts, such as heterogeneous catalysts, semiconductors, solar materials, thermoelectrics, and luminescence up-conversion materials. With recent advances in synchrotron X-ray[39] and neutron powder diffraction[40] techniques, structural information from inorganic materials can be obtained with unprecedented accuracy. Recently developed Monte Carlo simulation techniques enable detailed statistical investigation of total neutron scattering data[22,41,42] and are employed here for the first time on a phosphor material. X-ray absorption near-edge structure (XANES) and EXAFS yield crucial complementary information about the oxidation state(s) and local structural environments of the cerium substituent species. High-resolution solid-state nuclear magnetic resonance (NMR) spectroscopy can exploit the effects of paramagnetism of Ce^{3+} on the NMR parameters associated with nearby atomic sites, in combination with electron spin resonance (ESR) spectroscopy providing information that is complementary to scattering measurements on the local structures of Ce^{3+} ions. The range of techniques employed here enables detailed understanding of the local structure of Ce substituent ions in YAG and provides critical information for the rational design of new phosphor materials.

■ MATERIALS AND METHODS

Sample Preparation. Samples of $Y_{3-x}Ce_xAl_5O_{12}$ with x = 0, 0.02, 0.04, 0.06, 0.08, and 0.09 were prepared using conventional solid-state preparation methods.[43,44] Starting materials consisting of stoichiometric amounts of Y_2O_3 (Sigma-Aldrich, 99.9%), Al_2O_3 (Sumitomo AKP-50, >99.99%), and CeO_2 (Cerac, 99.9%), with 5% by mass BaF_2 (Sigma-Aldrich, 99.9%) and 0.5% by mass $NH4F$ (Sigma-Aldrich, 99.99%) as sintering agents (flux), were ground with an agate mortar and pestle, placed in alumina crucibles, and fired at 1500 °C for 5 h in an alumina tube furnace under 0.2 L/min 5% H_2/N_2 gas flow. Following standard procedures for phosphor preparation, we employed a fluoride flux. Samples prepared without flux required longer heating times and higher reaction temperatures but were otherwise indistinguishable from samples prepared using the flux, within the sensitivity limits of diffraction and NMR measurements. The amounts of flux and Ce were optimized by finding the concentrations that maximized the absolute emission intensity,

resulting in optimum values of 5 mass % BaF_2, 0.5 mass % NH_4F, and a Ce concentration of $x = 0.06$ ($Y_{2.94}Ce_{0.06}Al_5O_{12}$). The quantum efficiency of the optimized sample was determined to be 87%. Samples for XANES/EXAFS and total neutron scattering ($Y_{2.91}Ce_{0.09}Al_5O_{12}$) were prepared with stoichiometric amounts of Y_2O_3 (Sigma-Aldrich, 99.9%), Al_2O_3 (Sumitomo, 99.9%), and CeO_2 (Cerac, 99.9%), which was ground with an agate mortar and pestle, pressed into pellets, placed in alumina crucibles on a bed of sacrificial powder, and fired at 1600 °C for 96 h in an alumina tube furnace under a 0.2 L/min 5% H_2/N_2 gas flow. After the starting materials had been reacted, the phosphor cakes were ground with an agate mortar and pestle into fine powders.

Synchrotron X-Ray and Neutron Scattering. High-resolution synchrotron powder diffraction data were collected using the 11-BM beamline at the Advanced Photon Source (APS) at Argonne National Laboratory, using an average wavelength of $\lambda = 0.412154$ Å. Other details regarding the experimental setup can be found elsewhere.[39]

Neutron powder diffraction was performed on the HIPD and NPDF instruments at the Lujan Neutron Scattering Center at Los Alamos National Laboratory. Powder samples were placed in vanadium cans, and time-of-flight neutron data were collected at 295 K on the HIPD instrument from eight detector banks at ±45°, ±90°, ±119°, and ±148° 2θ. For the NPDF measurements, powder samples were placed in vanadium cans, and time-of-flight neutron data were collected at 15 and 295 K from four detector banks at 14°, 40°, 90°, and 153° 2θ.[45]

Crystal structures were refined using the programs XND[46] and the EXPGUI front end for the refinement program General Structure Analysis System (GSAS).[47] Simultaneous refinements to the X-ray and neutron scattering data were completed by adjusting the profile shapes and unit cells during the LeBail fits; refining neutron absorption coefficients, instrument parameters, and the backgrounds (10-term Chebyshev polynomial function); and then refining the atomic positions and finally the atomic displacement parameters and Y/Ce occupancies. Occupancies and atomic displacement parameters are usually strongly correlated in Rietveld refinements, so these were refined in alternate cycles. For joint X-ray and neutron refinements, the neutron data were scaled by a factor close to 1.2 so that the weighted contributions of the neutron and X-ray histograms were nearly equal. During the final refinement cycle, all appropriate free parameters were allowed to refine simultaneously. Crystal structures were visualized using the software VESTA.[48]

Neutron Total Scattering and Reverse Monte Carlo (RMC) Simulation. Time-of-flight (TOF) total neutron scattering on $Y_{2.91}Ce_{0.09}Al_5O_{12}$ was carried out at 295 K on the NPDF instrument at the Los Alamos Neutron Science Center at Los Alamos National Laboratory. The data were extracted using PDFgetN,[49] with $Q_{max} = 31$ Å. The uncertainty from the PDF measurement is around 0.1 Å ($\Delta r = \pi/Q_{max}$).[50] PDFgui was used to fit a symmetric model to the PDF out to 50 Å.[51] Reverse Monte Carlo simulations were run using RMCProfile version 6 and a $4 \times 4 \times 4$ supercell with 10 240 atoms.[52,53] These simulations were simultaneously constrained by the $S(Q)$ Bragg profile and the $G(r)$. All atom–atom distances were subject to a hard-sphere cutoff at 1.576 Å, since data at smaller distances consisted of termination ripples. RMC fits employed a maximum r of 20 Å. Ce and Y atoms were allowed to exchange positions with a 5% chance of each move being an atom swap. Eight runs were averaged for better statistics, and simulations were run for a total of approximately 915 Monte–Carlo sweeps.

X-Ray Absorption near Edge Structure (XANES) and Extended X-Ray Absorption Fine Structures (EXAFS). To determine the formal oxidation state of Ce, X-ray absorption near edge spectroscopy (XANES) experiments were performed in Sector 20, bending magnet beamline (PNC/XSD, 20-BM) of the Advanced Photon Source at the Argonne National Laboratory, Illinois. The pellet of the pure sample ($Y_{2.94}Ce_{0.06}Al_5O_{12}$ prepared with BaF_2 flux) was sandwiched between two layers of Kapton tape. The measurement was performed at room temperature in fluorescence mode using a four-element Vortex detector. Monochromatic X-rays were obtained using a Si(111) double crystal monochromator. The incident beam was

focused to a small spot (500 μm × 350 μm) using a Al_2O_3/Pt coated toroidal mirror.[54] A rhodium coated X-ray mirror was utilized to suppress higher order harmonics. Measurements on a CeO_2 standard, prepared by dusting finely ground powders on Kapton tape and stacking six layers together, were also performed using the unfocused beam in transmission mode. Measurements of CeO_2 were performed at low temperature, but is irrelevant to oxidation state determination.

Ce K-edge XANES studies were carried out at the sector 20-ID beamline at the Advanced Photon source at 295 K.[55] The fifth harmonic of the undulator was used along with full scanning of the undulator. The incident beam was monochromatized using a pair of Si(311) crystals. Higher order harmonics were suppressed by detuning the monochromator to reduce the incident X-ray intensity by approximately 15%. Argon-filled ion chambers were used for the I_o, I_t, and I_{ref} detectors. A cold pressed pellet of CeO_2 in BN was employed as an internal calibration for the alignment of edge position. The Ce K-edge in the $x = 0.09$ YAG:Ce sample was measured on a pure pellet of the sample in fluorescence geometry using a 13-element energy dispersive germanium detector, operated at a total count rate of ~80 kHz per element. The Y background fluorescence signal impinging the Ge detector was selectively reduced by using several layers of thin aluminum foil, and care was taken to account for dead time associated with saturation of the detector. The CeO_2 absorption edge was calibrated to 40.473 keV as previously measured.[56] Simulations of the data were performed using the Artemis code,[57] with fits performed in the k^2 regime; fits in other k^n regimes gave results in good agreement with the k^2 regime. The k-space range was 2.77 Å^{-1} to 16 Å^{-1}, giving a spacial resolution of about 0.1 Å. Ten variables were used with an estimated 25 independent points.

Solid-state ^{27}Al and ^{89}Y Nuclear Magnetic Resonance (NMR) Spectroscopy. High-resolution solid-state ^{27}Al and ^{89}Y magic-angle spinning (MAS) NMR spectroscopy were used to investigate the local structure of YAG:Ce. Single-pulse and T_1-filtered ^{27}Al NMR experiments were performed at room temperature on a Bruker AVANCE IPSO NMR spectrometer, with an 18.8 T narrow-bore superconducting magnet, operating at a frequency of 208.52 MHz for ^{27}Al nuclei, which are 100% naturally abundant. A Bruker 3.2 mm H–X–Y triple-resonance MAS probehead was used with zirconia rotors and Kel-F caps, with a MAS spinning rate of 24 kHz. The MAS resulted in heating of the sample, so that the temperature of the sample was somewhat higher than room temperature. The radio frequency (RF) pulse length of 2.7 μs and power level were calibrated to achieve a 15° ($\pi/12$) rotation of the net ^{27}Al magnetization to ensure quantitative measurements[58] and were calibrated with respect to the longitudinal spin–lattice relaxation time (T_1) to ensure that the spectra were fully quantitative (recycle delay of 40 s). An external AlN sample was used as a spin-counting standard to compare the absolute ^{27}Al signal intensity with results from elemental analyses, which confirmed 100% visibility of ^{27}Al nuclei in all samples measured. A total of 192 transients were collected for the single-pulse ^{27}Al NMR spectra, and chemical shifts were referenced to 1 M $Al(NO_3)_3$ (aq.) at 0 ppm.

^{27}Al spin–lattice relaxation-time behaviors of the YAG:Ce samples were established by using complementary 1D saturation-recovery and T_1-filtered ^{27}Al MAS NMR spectra. 1D saturation-recovery ^{27}Al MAS NMR spectra were acquired for a range of recovery delays, τ, between 0.05 and 70 s on a Bruker AVANCE IPSO NMR spectrometer, with an 11.7 T wide-bore superconducting magnet, operating at a frequency of 130.28 MHz for ^{27}Al nuclei. The number of transients was scaled with the delay times and ranged from 24 to 1024, with more transients acquired for shorter delay times. A Bruker 4 mm H–X–Y triple-resonance MAS probehead was used with zirconia rotors and Kel-F caps, with a MAS spinning rate of 14 kHz. A RF pulse length of 2.51 μs was calibrated with the power level for a 90° rotation of the net magnetization of six-coordinate ^{27}Al nuclei, and a 400-pulse saturation train with 2 μs between saturation pulses was used with a 0.1 s recycle delay. The long saturation train was not rotor-synchronized, leading to a saturation of the central and satellite transitions, minimizing effects from population transfer between ±5/2 and ±3/2 to ±1/2 Zeeman levels.[59,60] 1D T_1-filtered ^{27}Al MAS NMR spectra (measured on the

18.8 T NMR spectrometer) were acquired with two consecutive ^{27}Al 90° pulses, followed by a time delay, t_{T_1} = 15 s, and then another ^{27}Al 90° pulse before detection to suppress six-coordinate ^{27}Al signals from species with spin−lattice relaxation times shorter than the respective t_{T_1} = 15 s values. The 1D T_1-filtered ^{27}Al MAS NMR spectra were scaled using an appropriate constant $c > 1$ to account for decreased signal intensity due to T_1 relaxation effects, which allows for the remaining signals to be normalized for comparison with the single-pulse ^{27}Al spectrum.

High-field solid-state ^{27}Al NMR measurements were recorded on a Bruker Avance III 1 GHz spectrometer operating at a ^{27}Al Larmor frequency of 260.7 MHz. A 1 M aqueous solution of $Al(NO_3)_3$ was used as the chemical shift reference. Spectra of the YAG:Ce material were acquired with a 1.3 mm HX probe at 60 kHz MAS. The T_1 relaxation time constants were measured using a saturation-recovery experiment comprising a saturation sequence of 30 pulses separated by delays of 3 ms and a recovery delay taking 27 values varying from 0 to 150 s. The 1D spectra were acquired using a one-pulse sequence with 288 scans, a recycle delay of 35 s (x = 0.09) and 110 s (x = 0.00), and an excitation pulse of 50 kHz RF field amplitude and 1.67 μs duration.

Solid-state ^{89}Y NMR experiments were performed at the U.S. National High Magnetic Field Laboratory in Tallahassee, Florida, on a narrow-bore Magnex 19.6 T magnet with a Bruker console, operating at a frequency of 40.804 MHz for ^{89}Y nuclei, which are 100% naturally abundant. Data were collected under MAS conditions of 6 kHz and room temperature using a Samoson 7 mm H-X triple-resonance MAS probehead with zirconia rotors and Kel-F caps. RF pulses with a 4 μs length were used with a recycle delay of 140 s, and 200 transients were signal averaged. Chemical shifts were referenced to 1 M YCl_3 (aq.).

Solid-state NMR spectra were modeled using the simulation program dmfit;[61] ^{27}Al peaks from octahedrally coordinated Al^{VI} species were fit with Gaussian lineshapes. Relative populations of ^{27}Al species were found by fitting the largest signal associated with the $+1/2 \rightarrow -1/2$ central transition and the two nearest spinning sidebands for each signal, then subtracting the average integrated intensity of the two spinning sidebands from the integrated intensity of the central peak. The T_1 relaxation times of ^{27}Al^{VI} nuclei were found by fixing the peak widths and peak positions of the fit from the single-pulse ^{27}Al spectra, then fitting the amplitude of the peaks for the spectrum determined at each delay time.

Electron Spin Resonance (ESR) Spectroscopy. ESR spectra were collected on a Bruker X-Band ESR spectrometer (ν = 9.486 GHz), equipped with a helium flow cryostat. Samples were placed in quartz tubes, and spectra were acquired at temperatures ranging from 4 to 40 K. The set of linewidths as a function of temperature of the peak at 2480 G were fit with the curve fitting tool in MATLAB. Spectral simulations employed the easyspin code implemented in MATLAB,[62] with a correction included for field-dependent relaxation effects. The g_x peaks were fit with Gaussian lineshapes by using the program DMFIT.[61]

■ RESULTS AND DISCUSSION

Influence of Ce^{3+} Substitution on the Average Crystal Structure. High-resolution synchrotron X-ray diffraction enables detailed examination of sample purity as well as investigation of small changes in the average structure of ordered materials and has been used here to probe accurately the effect of the small amount of Ce substitution on the average structure of YAG. The X-ray scattering data show that the materials are phase pure, with small $YAlO_3$ impurities of less than 1 mol % in some samples.[63] Rietveld refinements of synchrotron X-ray data acquired for different YAG:Ce materials with systematically varied Ce concentrations, $Y_{3-x}Ce_xAl_5O_{12}$ with x = 0, 0.02, 0.04, 0.06, 0.08, and 0.09 (data shown in Figure 1b), reveal a small linear increase in the YAG unit cell (Figure 1a) lattice parameter with Ce^{3+} substitution (Figure 1c). The linear increase in the unit cell parameter with
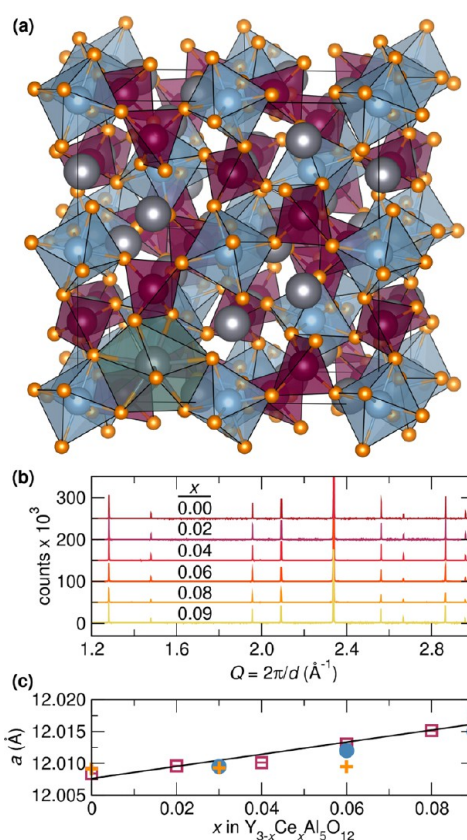

Figure 1. (a) The YAG structure looking down the a axis, with red, blue, gray, and orange spheres representing four-coordinate Al (Al^{IV}), six-coordinate Al (Al^{VI}), Y, and O atoms, respectively. (b) Synchrotron X-ray diffraction patterns of $Y_{3-x}Ce_xAl_5O_{12}$ acquired at 295 K for x as indicated. (c) The unit cell parameter from Rietveld refinement (exemplary refinement shown in Figure 2a) as a function of Ce concentration, x (red open squares). Error bars from the estimated standard deviation are shown for the data collected here but are smaller than the symbols. The Végard law is followed,[64,65] showing a very small linear expansion of the unit cell with Ce substitution. "+" symbols represent data from Robbins et al.,[66] and filled circles represent data from Tien et al.[67]

substitution of the larger Ce atom (relative to Y) follows the Végard law,[64,65] suggesting that the majority of Ce from the starting materials is being substituted into the YAG lattice. It additionally suggests that the expansion of the lattice around Ce is distributed over length scales on the order of the unit cell. The change in unit cell parameter with Ce substitution is very small; the unit cell parameter increases by only 0.056% from x = 0 to x = 0.08 Ce substitution in $Y_{3-x}Ce_xAl_5O_{12}$.

Rietveld refinement of synchrotron X-ray and neutron diffraction data, as shown in Figure 2a,b,c, yields unit cell parameters, the oxygen atom positions, and Ce occupancies as given in Table 1. As the temperature is decreased from 295 to 15 K, a very small contraction of about 0.15% in the unit cell is observed, along with a decrease in atomic displacement parameters (ADPs). A small change in the unit cell parameter with temperature is consistent with previous measurements of the thermal expansion of YAG, which show the thermal expansion parameter, α, to be on the order of 1×10^{-6} K^{-1}.[68] This implies that the structure is very rigid, which is additionally supported by the unusually small values of the atomic displacement parameters found here. Since Y and Ce have sufficiently different neutron scattering lengths (4.03 barn
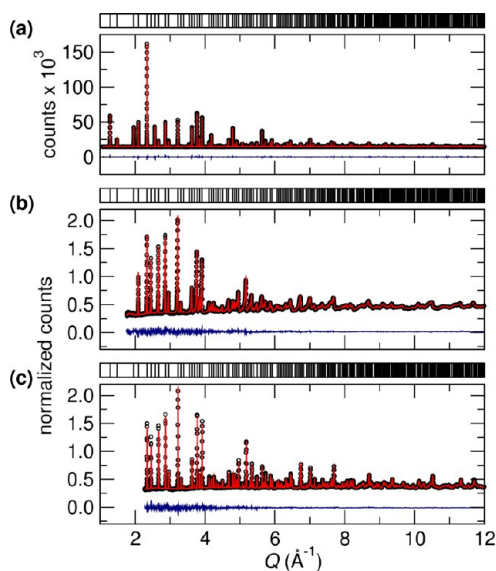
Figure 2. Simultaneous Rietveld refinement of (a) synchrotron X-ray scattering data and (b) time-of-flight neutron scattering data acquired at 295 K of $Y_{2.94}Ce_{0.06}Al_5O_{12}$ and (c) Rietveld refinement of time-of-flight neutron scattering data at 15 K of $Y_{2.92}Ce_{0.08}Al_5O_{12}$. The expected reflection positions are shown above each plot.

This can be investigated by fitting the PDF with a least-squares method using a periodic unit cell.[51] The PDFgui least-squares fit to the 295 K neutron PDF of $Y_{2.91}Ce_{0.09}Al_5O_{12}$ out to 50 Å, shown in Figure 3a, fits the data well and yields the correlated

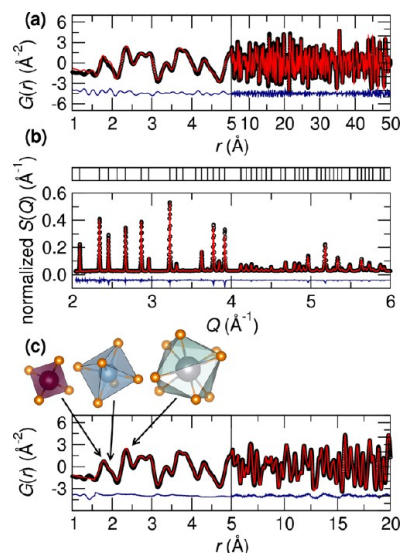**Figure 3.** Time-of-flight neutron scattering data of $Y_{2.91}Ce_{0.09}Al_5O_{12}$ acquired at 295 K with (a) PDFgui least-squares fit of $G(r)$ with a R_{wp} of 9.1% and reverse Monte Carlo fits of (b) $S(Q)$ and (c) $G(r)$. The expected peak positions for $S(Q)$ are shown above b. Polyhedra are shown in the inset above c, with arrows denoting the corresponding peaks in the PDF for the (from left to right) Al^{IV}, Al^{VI}, and eight-coordinate Y sites.

and 7.15 barn for Ce and Y, respectively), the Ce/Y occupancies can be refined stably. The Ce occupancies shown in Table 1 closely follow the nominal compositions employed in the preparation. Ascertaining that the majority of the Ce has indeed been incorporated into the lattice rules out the possibility of impurity phases that might quench luminescence, and this is further supported by the ^{27}Al NMR results discussed below.

The Local Ce^{3+} Environment from Scattering. Rietveld analysis is a powerful tool for investigating the average structure of materials, but it cannot probe features associated with the local structure, such as correlated atomic motion that arises from stiff forces of nearest-neighbor bonds.[50] These stiff forces relate to the interatomic potentials, and hence the extent to which a lattice will deform when a large substituent ion such as Ce^{3+} is incorporated in YAG. The peak width of nearest-neighbor features in the pair distribution function (PDF) contains information on vibrations associated with stiff bond-stretching forces and the resulting correlated atomic motions.

motion parameter δ_2, which is related to the width of nearest-neighbor peaks in the PDF. Essentially, the δ_2 parameter is larger for stiffer bonds. The value of δ_2 obtained here is 2.3(3) Å^2, larger than the value of 1.8(1) Å^2 reported for Al_2O_3 on the ARCS beamline,[69] which further supports the hypothesis that the stiff near-neighbor bonds in YAG exhibit a high degree of rigidity.

The local structure near the Ce substituent species in YAG is closely related to the optical properties of YAG:Ce, because the bond length and orientation of the Ce–O bonds will determine the 5d energy levels, and hence the excitation and emission energies. The symmetry constraints of least-squares refinement of PDF data using a periodic unit cell prohibit selectively

Table 1. Crystallographic Parameters of $Y_{3-x}Ce_xAl_5O_{12}$ from Rietveld Refinement of Synchrotron X-Ray, HIPD Neutron, and NPDF Neutron Scattering Data^a

T (K)	15		295		
	$x = 0$	$x = 0.08$	$x = 0$	$x = 0.06$	$x = 0.09$
beamline(s)	NPDF	NPDF	11-BM, HIPD	11-BM, HIPD	11-BM, NPDF
R_p (%)	1.39	1.41	6.17 (X-ray)	5.74 (X-ray)	11.2 (X-ray)
			1.11 (neutron)	1.09 (neutron)	1.97 (neutron)
			2.27 (overall)	2.19 (overall)	6.07 (overall)
a (Å)	11.99067(2)	11.99795(2)	12.008476(3)	12.013001(5)	12.01558(3)
O x	0.28049(3)	0.28056(3)	0.280598(9)	0.28058(1)	0.28062(2)
O y	0.10103(3)	0.10099(2)	0.10092(1)	0.10099(1)	0.10094(2)
O z	0.19914(3)	0.19922(2)	0.199330(9)	0.19946(1)	0.19942(2)
refined Ce_x		0.07(2)		0.09(3)	0.10(1)

^{a}Ce_x refers to the amount of Ce in $Y_{3-x}Ce_xAl_5O_{12}$. All refinements were carried out with the $Ia\bar{3}d$ space group (#230). Exemplary Rietveld refinements are shown in Figure 2. The estimated standard deviations for the last significant digit are given in parentheses.

investigating the local coordination environments of the Ce substituent ions. The Ce local environments are hypothesized to be distinct from that of Y but not highly distorted because of the stiff nearest-neighbor bonds and rigid structure. Reverse Monte Carlo (RMC) simulations, which simultaneously model the local and long-range structure of a material,[52,53,70,71] enable selective investigation of the structure around Ce because its local coordination is no longer constrained by symmetry to be the same as that of Y. As mentioned previously, Y and Ce have neutron scattering lengths which allow for Ce to be distinguished from Y in the simulations. The results of the RMC fits to the neutron data, shown in Figure 3b,c and as the 4 × 4 × 4 supercell collapsed onto one unit cell in Figure 4a,
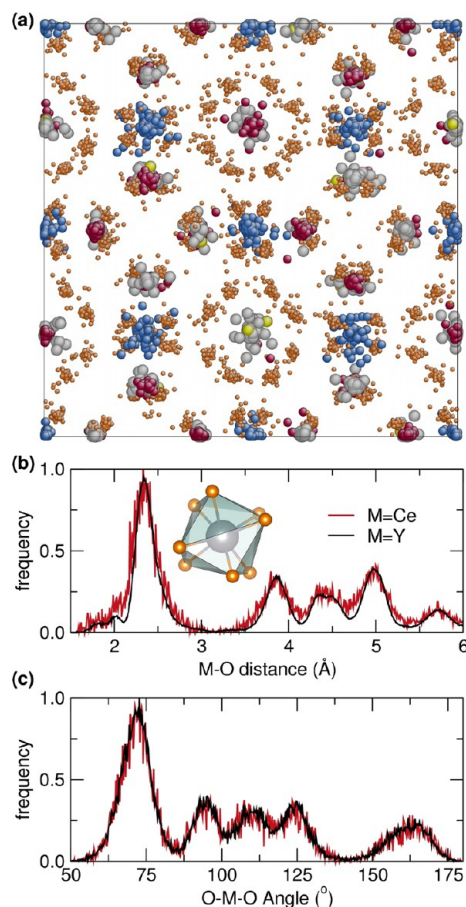
Figure 4. (a) View down the *a* axis of the 4 × 4 × 4 RMC supercell of $Y_{2.91}Ce_{0.09}Al_5O_{12}$ collapsed onto a single unit cell, simulated with 915 MC sweeps to neutron scattering data collected at 295 K. (b) Metal–oxygen distance distributions from the average of eight reverse Monte Carlo fits of 295 K time-of-flight neutron scattering data. (c) Oxygen–metal–oxygen bond angle distributions for Y and Ce in $Y_{2.91}Ce_{0.09}Al_5O_{12}$. The inset shows an eight-coordinate Y–O polyhedron from the average YAG structure. Blue, red, gray, yellow, and orange spheres in a represent Al^{VI}, Al^{IV}, Y, Ce, and O atoms, respectively. Fits to the data from the simulation are shown in Figure 3b,c.

exhibit a distribution of Ce–Ce distances similar to Y–Y distances (Supporting Information, SI, Figure S2). This supports a random distribution of Ce in the YAG lattice, consistent with ^{27}Al NMR and ESR results discussed later.

Examination of the M–O (M = Ce, Y) distance histograms and O–M–O angle distributions from the RMC simulation of

$Y_{2.91}Ce_{0.09}Al_5O_{12}$ in Figure 4b,c suggests that the much larger Ce^{3+} atom adopts effectively the same local environment as the smaller Y^{3+} atom in YAG, with essentially identical M–O distance and O–M–O angle distributions. The lack of distortion in the O–Ce–O bond angles is consistent with the rigid bonds found from the large δ_2 from the PDFgui fit and is consistent with a previous *ab initio* study.[37] Average Ce–O distances of 2.31 Å and 2.44 Å found here are slightly smaller than the values of 2.40(2) Å and 2.50(2) Å from the EXAFS results presented later. The nearly imperceptible distortion of the lattice around Ce^{3+} is consistent with the small increase in unit cell parameter found from Rietveld analysis in Figure 1b, since a larger local distortion around Ce would be expected to expand the lattice by a greater amount. It is also consistent with the highly stiff nearest-neighbor bonds determined from the width of nearest-neighbor peaks in the PDF. The nearly identical Ce–O and Y–O distance distributions imply that Ce^{3+} is severely compressed in the YAG lattice, since the Shannon–Prewitt ionic radius of eight-coordinate Ce^{3+} (1.143 Å) is larger than the radius of eight-coordinate Y^{3+} (1.019 Å).[72] The average bond valence sum[73,74] from the simulations yields an estimate of the extent of overbonding from the short Ce–O bonds. The average Ce bond valence sum was determined to be 4.0 ± 0.1, which is much higher than expected for the nominal valence state of 3 and the average bond valence sum of Y of 3.1 ± 0.1. Prior work using a point-charge model has shown the d-orbital crystal-field splitting (Dq) is related to the Ce^{3+}–O bond length as $1/r^5$.[75] The compression of the Ce^{3+} local environment observed here is therefore what leads to the unusually large crystal-field splitting of the Ce 5d states in YAG.[26,28]

The bond valence sum of 4.0 found from RMC simulations does not support Ce in the +3 state, as is required for the optical properties. XANES offers a direct method for measuring oxidation state(s) of Ce, which is critically important to the optical properties of YAG:Ce since Ce^{4+} ions can quench Ce^{3+} luminescence.[76] The shape of the Ce L_3 XANES spectra is a strong fingerprint of the formal oxidation state of cerium. Ce L_3-edge XANES data collected on $Y_{2.94}Ce_{0.06}Al_5O_{12}$ at 295 K, shown in Figure 5a, reveal that the Ce in YAG:Ce produces a single, strong peak (white line resonance) around 5.726 keV, consistent with Ce^{3+}.[77] Conversely, the spectrum of formally tetravalent Ce in CeO_2 in Figure 5a shows a double peaked spectrum, characteristic of Ce^{4+}.[78] This indicates that the great majority of the Ce in YAG:Ce materials investigated here is in the +3 state. The K-edge XANES in Figure 5b shows that the absorption edge lies at 40.469 keV, a lower energy than the Ce absorption edge in CeO_2 at 40.473 keV, adding support that the majority of Ce in YAG:Ce is in the +3 state.[56] Interestingly, most compounds with Ce^{3+} have Ce K-edge XANES absorption edges at least 7 eV lower than CeO_2,[79] but the absorption edge of Ce in YAG is only 4 eV lower in energy. The results here from XANES are further supported by the solid-state ^{27}Al NMR results below, which show that the vast majority of the Ce atoms in the lattice are reduced to Ce^{3+}.

The short Ce–O bonds found from the RMC simulations can be directly probed by EXAFS. A fit to the EXAFS data of $Y_{2.91}Ce_{0.09}Al_5O_{12}$ shown in Figure 5c,d (R-factor of 1.55%) reveals that the Ce–O bond distances do expand somewhat from the average structure Y–O distances of 2.31 Å and 2.44 Å, with Ce–O distances of 2.40(2) Å and 2.50(2) Å. The Ce–O distances found here are slightly larger compared to the values from two theoretical studies of 2.373 and 2.468 Å[38] and 2.370
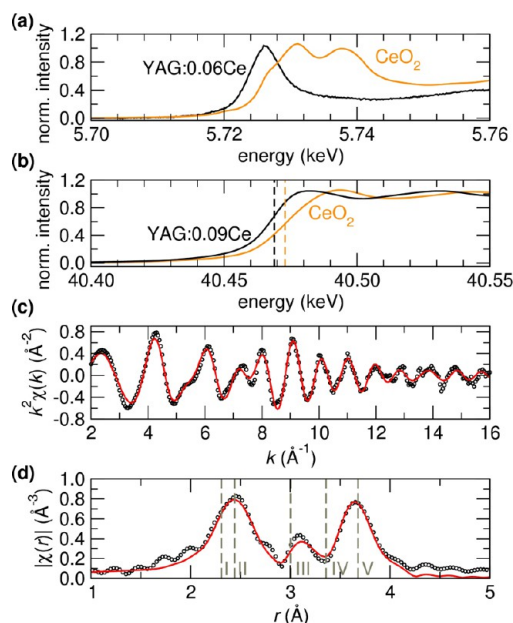
Figure 5. (a) Ce L-edge XANES spectra of $Y_{2.94}Ce_{0.06}Al_5O_{12}$ and CeO_2. (b) K-edge XANES spectra of $Y_{2.91}Ce_{0.09}Al_5O_{12}$ and CeO_2. (c) EXAFS signal acquired at 295 K with fit. (d) Corresponding EXAFS Fourier transform and fit. The vertical dashed lines in b indicate the absorption edges for $Y_{2.91}Ce_{0.09}Al_5O_{12}$ at 40.469 keV and CeO_2 at 40.473 keV.[56] The vertical dashed lines in d indicate the Y/Ce–X (X = O, Al, Y) interatomic distances from Rietveld refinement of 295 K neutron scattering data of the same sample, with I, II, III, IV, and V corresponding to Y/Ce–O1, Y/Ce–O2, Y/Ce–Al^{IV}, Y/Ce–Al^{VI}, and Y/Ce–Al^{IV}/Y distances, respectively. A phase shift was applied to the data in d after fitting, based on the first Ce–O coordination shell.

Table 2. Interatomic Ce–X Distances for $Y_{2.91}Ce_{0.09}Al_5O_{12}$ Determined from Rietveld Refinement and EXAFS Data at 295 K[a]

		Ce–X Distance (Å)	
X	N	Rietveld[b]	EXAFS[c]
O1	4	2.3090(2)	2.40(2)
O2	4	2.4401(2)	2.50(2)
Al$_t$	2	3.00238(2)	3.05(1)
Al$_o$	4	3.35677(2)	3.41(1)
Al$_t$	4	3.67715(2)	3.71(1)
Y	4	3.67715(2)	3.71(1)

[a]The estimated standard deviations are shown in parentheses for the last significant digit. [b]The Rietveld values were obtained from simultaneous Rietveld refinement of synchrotron X-ray and time-of-flight neutron scattering data (Figure S3, SI). [c]The EXAFS fit also included the next two coordination shells around Ce (Ce–O pairs), but the distances did not differ significantly from the Rietveld refinement.

and 2.441 Å[37] but agree well with the RMC results and previous results from lower-resolution (smaller k_{max}) Ce K-edge EXAFS, which found Ce–O distances of 2.38(1) Å and 2.52(2) Å.[36] Additionally, the previous EXAFS study used YAG with a lower Ce concentration ($x = 0.03$) than this investigation ($x = 0.09$), demonstrating that the local structural distortion around Ce substituent atoms is not strongly dependent on the Ce concentration in YAG. This means that previous findings of a red-shift in emission with increasing Ce concentration[30] are likely not due to expanding Ce–O bonds with increasing Ce content (which would decrease the crystal-field splitting) but are instead probably due to energy transfer from excited Ce^{3+} ions to nearby Ce^{3+} ions with lower 5d energies.

The high resolution obtainable from Ce K-edge EXAFS enables a precise investigation of the Al and Y atoms near Ce in the structure and reveals that the Ce–Al and Ce–Y distances in the first few Ce coordination shells do significantly deviate from the average structure Y–Al and Y–Y distances, shown in Table 2. This shows that the expansion of the lattice around Ce^{3+} ions in YAG is not limited to the first few coordination shells of O and Al atoms but in fact spans five or more coordination shells. This offers a satisfying explanation as to why the lattice expands with the addition of Ce; the distortions are not contained within a short distance but are spread out over the structure. This 3% change in the first coordination sphere of Ce–O translates to an expansion of the unit cell on the order of 0.01% seen in the synchrotron X-ray results, due to spreading of the distortion over the YAG lattice. Past the Ce–Y coordination shell at around 3.7 Å, the distortions become imperceptible to the EXAFS measurement.

The small 3% expansion of the Ce–O bond distances, compared with the average structure Y–O distances decreases the Ce bond valence sum[73,74] of 4.0 ± 0.1 to 3.3 ± 0.1, which indicates that Ce is tightly compressed in the YAG:Ce lattice. The 3% increase in Ce–O bond length compared to the Y–O bond length is unusual, since Ce is much larger than Y, with a 12% larger ionic radius for eight-coordinated Ce^{3+} compared with Y^{3+}. In the $Zn_{1-x}Mg_xO$ system, for example, a 5% smaller Mg (by ionic radii) was found to have about 2% shorter bonds than Zn.[80] The unusually small distortion around Ce in YAG is what causes the large crystal-field splitting of Ce, since increased orbital overlap of the O anions with Ce is expected. In fact, the crystal-field splitting of YAG:Ce is one of the largest of most oxide based phosphors.[81] The short Ce–O bonds are what makes blue absorption and yellow emission possible in YAG:Ce; whereas other phosphors with a similar coordination geometry (but purportedly less compression of Ce–O bonds), such as $Sr_2LiSiO_4F:Ce^{3+},Li^{+}$[82] and $Sr_3SiO_5:Ce^{3+}$,[83] have emission colors that are more blue-shifted than YAG:Ce. The high compression of the Ce^{3+} sites in this structure also suggests a reason for the relatively small intrinsic limit of Ce substitution, which is usually close to $x = 0.09$ to 0.12 in $Y_{3-x}Ce_xAl_5O_{12}$ from conventional ceramic solid-state preparation. This is an important parameter, since it defines the highest value of the optical extinction coefficient of YAG:Ce, which in turn determines how much phosphor must be used in a phosphor-converted white lighting LED device.

Analysis of the Atomic Displacement Parameters. Vibrational characteristics of a crystalline lattice, which relate to nonradiative recombination in phosphors, can be accurately probed by Rietveld refinement of neutron scattering data. Whereas X-ray scattering exhibits form factors that decay rapidly with increasing Q, neutron scattering intensities essentially remain constant with increasing Q,[85] allowing for precise determination of atomic displacement parameters (ADPs). The ADPs represent positional uncertainty of the atoms in a structure, which may result from thermal motions and static disorder in a crystalline material. Careful investigation of the ADPs of a phosphor material can therefore yield insights into the crystallinity and vibrational properties of that material, which relates to the quantum efficiency because defects and phonons play a major role in quenching mechanisms of phosphors.

The ADPs found here, shown for $Y_{2.94}Ce_{0.06}Al_5O_{12}$ with 99% probability in Figure 6a, are notably small. More specifically, the
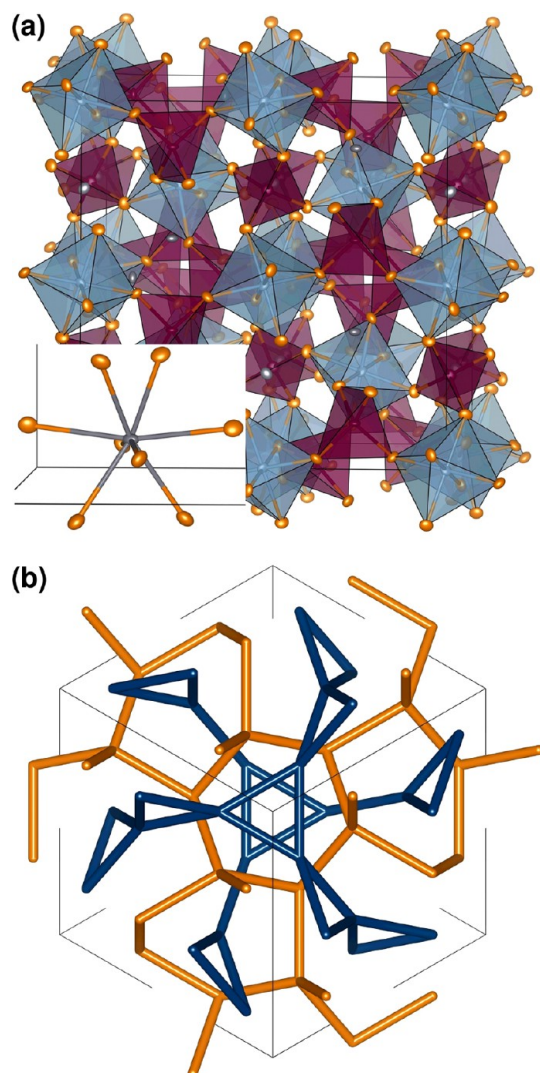

Figure 6. (a) View down the *a* axis of the Rietveld-refined structure of $Y_{2.94}Ce_{0.06}Al_5O_{12}$ at 295 K from synchrotron X-ray scattering data and neutron scattering data, with the inset showing an expanded view of a Y atom with bonds drawn to the surrounding O atoms. 99% probability atomic displacement parameters are shown as red, blue, gray, and orange ellipsoids, which represent Al^{IV}, Al^{VI}, Y, and O atoms, respectively. (b) View down the (111) face of the YAG unit cell, showing the interpenetrating networks of Y and Al, which form a double-gyroid structure. The blue cylinders are drawn between Y atoms, while the orange cylinders connect Al^{IV} atoms. The Al^{VI} atoms were excluded from b for clarity.

YAG:Ce ADPs are slightly smaller than those of yttrium–aluminum perovskite[86] and the spinel $MgAl_2O_4$[87] and only about half the values seen for the perovskite $CeAlO_3$.[88] It is well-known that ADPs are a catch-all term that include effects of site and occupancy disorder, which means the values here are an upper bound on the true ADP values. The mean-square relative displacements (MSRDs) from the EXAFS fit are smaller than the ADPs found from Rietveld analysis of the same sample. However, caution must be taken when comparing ADPs to MSRDs, since the MSRDs include correlated atomic motions and tend to be smaller than corresponding ADPs—especially for the first coordination shell.[89] The Debye

temperature θ_D, which provides an estimate of the temperature at which all vibrational modes of a crystal are activated, can be calculated from the isotropic ADPs as shown in Table 3.[84] Small average atomic displacement parameters imply high Debye temperatures and *vice versa*. This suggests that fewer phonon modes are accessible at a given temperature in a rigid crystal lattice with small ADPs, compared to a floppy crystal lattice with large ADPs. For example, the average isotropic atomic displacement parameter (U_{iso}) measured here for YAG at 295 K is approximately 0.0093 $Å^2$, corresponding to the previously measured θ_D = 760 K.[90] In another structure where such an analysis has been carried out, $KGd(WO_4)_2$, the smaller θ_D of 580 K[90] corresponds to a larger average U_{iso} measured as 0.020 $Å^2$.[91] The smaller number of accessible phonon modes reflected in the high Debye temperature is believed to play a key role in the high quantum efficiency of YAG:Ce.

Furthermore, the tight compression of Ce in YAG found from the RMC and EXAFS results and the small MSRDs near Ce are possibly at the heart of the low probability of nonradiative transitions and high quantum efficiency of YAG:Ce. Nonradiative combination is thought to occur through excitation of the 5d state to the conduction band[92] or defect states, or from thermal excitation of the excited electron to the crossover point of the potential wells of the 5d and 4f levels.[93] Small ADPs of the average structure and small MSRDs around substituted Ce ions indicate a smaller number of phonon levels accessible through thermal activation that aid in quenching excited Ce^{3+} electrons nonradiatively, thereby decreasing the probability of nonradiative transitions.[93] This is complemented by the large band gap of YAG of around 6.5 eV,[94] in addition to the 1.24 eV energy gap between the lowest-energy Ce^{3+} 5d state and the YAG conduction band.[95] This indicates materials with rigid bonds, reflected by small ADPs, a high Debye temperature, and small MSRDs around a substituent luminescent ion, should be sought after for high-efficiency phosphors. This is consistent with a study by Brgoch et al., which demonstrated that the Debye temperature correlates well with phosphor quantum efficiencies.[96]

As shown in Table 3, increasing Ce concentration correlates with increasing ADPs and a decreasing θ_D. This is due to greater static disorder in the structure from distortions caused by Ce substitution, as well as an increase in the low-frequency and other phonon modes due to the addition of heavier Ce atoms into the structure (mass contrast) which increases the low-frequency Einstein modes available to the system. Hitherto, a decrease in quantum efficiency with increasing activator ion concentration has been attributed to energy transfer between activator ions but also appears to result from an increased number of accessible phonon modes at a given temperature for higher Ce concentrations. The θ_D temperatures of around 600 to 700 K for the Ce-substituted YAG materials correspond well with intrinsic quenching temperatures greater than 600 K for YAG substituted with small amounts of Ce,[30] and the high θ_D is also consistent with the observation of a 200 cm^{-1} dominant phonon mode in YAG:Ce.[30,97] This demonstrates that for a phosphor material to have a high quantum efficiency, it should be a rigid structure, as reflected in a high θ_D and small ADPs.

The high θ_D from the rigid lattice and thus the high quantum efficiency exhibited by YAG is of course closely related to its structure. The Y–Y and Al–Al connectivities form a double-gyroid structure through Y–O–Y and Al^{IV}–O–Al^{VI}–O–Al^{IV} pathways (Al^{IV} and Al^{VI} represent four- and six-coordinate Al atoms, respectively), shown as a simplified version of Y–Y and

Table 3. Isotropic Atomic Displacement Parameters of $Y_{3-x}Ce_xAl_5O_{12}$ from Rietveld Refinement and Least-Squares Fit to the PDF Fits of Neutron and X-Ray Scattering Data[a]

T (K)	15		295				
	$x = 0$	$x = 0.08$	$x = 0$	$x = 0.06$	$x = 0.09$	$x = 0.09$	$x = 0.09$
data type	NPDF		HIPD neutron	11-BM X-ray	NPDF	NPDF (1 Å to 50 Å)	
method	Rietveld	Rietveld	Rietveld	Rietveld	Rietveld	PDF	EXAFS
Y/Ce B_{iso} (Å^2)	0.16(1)	0.20(1)	0.178(3)	0.227(4)	0.36(1)	0.43(6)	0.36(4)
Al$_o$ B_{iso} (Å^2)	0.12(1)	0.20(1)	0.215(4)	0.250(5)	0.33(1)	0.38(4)	0.2(1)
Al$_t$ B_{iso} (Å^2)	0.19(3)	0.23(2)	0.21(1)	0.22(1)	0.34(2)	0.39(2)	0.2(1)/0.36(4)[b]
O B_{iso} (Å^2)	0.25(1)	0.30(1)	0.255(5)	0.295(6)	0.43(1)	0.51(6)	0.36(4)
θ_D (K)	634	506	853	760	628	578	690

[a]All refinements used the $Ia\bar{3}d$ space group (#230). The numbers reported for the EXAFS fit are mean-square relative displacement factors. The Debye temperatures shown, θ_D, are the average of the values calculated from the isotropic atomic displacement parameters.[84] The full tables of anisotropic displacement parameters can be found in the SI, Table S1. Estimated standard deviations for the last digits of parameters are given in parentheses. [b]The two atomic displacement parameters are for the third and fifth coordination shells around Ce, respectively.

Al^{IV}−Al^{IV} connectivities in Figure 6b. The Al^{IV} and Al^{VI} network is formed by corner sharing of the Al polyhedra, which would not typically happen with elements that have a higher charge and similar coordination numbers, such as four-coordinate Si, following Pauling's fourth crystal-chemical rule for ionic crystals.[98] The high connectivity of the YAG lattice decreases the degrees of freedom available for phonon modes, especially local Einstein-like modes. Furthermore, the tightly packed structure results in high energies associated with large displacements of atoms, requiring high temperatures to activate many of the phonon modes. This is consistent with the high intrinsic quenching temperature of YAG:Ce of over 600 K,[30] as well as the high Debye temperature of YAG well over 600 K. Another beneficial contribution to the high θ_D of YAG:Ce is the chemical simplicity and high structural symmetry of the material; with only four types of atoms and four crystallographic sites, there are fewer phonon modes than would otherwise be present with more distinct atomic species and/or sites. This chemical simplicity, high structural symmetry, and rigid structure leave few vibrational modes to aid in nonradiative transitions of the unpaired Ce^{3+} electron under ambient conditions, which largely account for the structural origins of the high quantum efficiencies of YAG:Ce.

Ce^{3+} Paramagnetic Effects on Proximal ^{27}Al and ^{89}Y Nuclei. Compositions and structures in the immediate vicinities of the Ce^{3+} activator ions are crucial to the photoluminescence properties of YAG:Ce. Such local structures can be elucidated by solid-state NMR spectroscopy, which is sensitive to the bonding environments of NMR-active ^{27}Al and ^{89}Y atoms near the Ce^{3+} substituent ions. Information that can be obtained includes the relative populations of distinct types of ^{27}Al or ^{89}Y atoms, which can be compared to and correlated with results from scattering. In particular, the unpaired electron in the 4f shell of Ce^{3+} alters the local magnetic field of nearby nuclei, enabling a selective probe of the YAG lattice around the Ce^{3+} substituent ions. This is analogous to the use of paramagnetic contrast agents that have been used to enhance the resolution of liquid-state NMR spectra.[99] In the case of liquid-state NMR, the contrast agents are external and influence most or all of the NMR-active nuclei under investigation. However, in the case of YAG:Ce, the contrast agent is internal, i.e. an intrinsic part of the structure of the material under investigation. This results in effects of the paramagnetic ion on the surrounding lattice that depend on the proximities of atoms to the rare-earth substituents. Due to the quadrupolar nature of

spin-5/2 ^{27}Al nuclei, solid-state ^{27}Al NMR spectra yield the quadrupolar coupling constant (C_Q) and the asymmetry parameter (η_Q). C_Q relates to the magnitude of the quadrupolar interaction and determines the width of a corresponding NMR signal, while η_Q is related to the symmetry of the electric field gradient and determines the line shape.[100] For YAG, these have previously been determined to be C_Q = 6 MHz for Al^{IV} and C_Q = 0.6 MHz for Al^{VI}, with η_Q = 0 for both Al sites.[101,102] This results in a much broader peak associated with the Al^{IV} species, due to the lower symmetry of the crystallographic site compared with Al^{VI} species, making analysis of Al^{IV} sites more challenging. However, the second-order quadrupolar interaction primarily responsible for broadening of the ^{27}Al NMR peaks can be mitigated by using very high magnetic fields.[100]

Solid-state ^{27}Al NMR spectra were consequently acquired at 18.8 T, under conditions of magic-angle spinning (MAS), as shown in Figure 7a for $Y_{3-x}Ce_xAl_5O_{12}$ with x = 0, 0.02, 0.04, 0.06, and 0.08. The 1D single-pulse ^{27}Al MAS spectra exhibit resolved signals at 77 ppm and 1.3 ppm, associated with the ^{27}Al^{IV} and ^{27}Al^{VI} sites, respectively. The relative integrated signal intensities of the two types of ^{27}Al species from all samples agree well with the expected 3:2 ratio for the Al^{IV}:Al^{VI} species in the YAG structure. The well-defined second-order quadrupolar lineshapes and relative intensities are consistent with crystalline and single-phase materials and are in good agreement with previous measurements of unsubstituted YAG.[101,103,104] As Ce is added, broadening of both signals is observed, and another ^{27}Al^{VI} signal appears near −15 ppm, associated with a distinct Al^{VI} species that has been previously regarded as an impurity;[105] however, the signal is consistent with ^{27}Al^{VI} nuclei in the first coordination sphere of paramagnetic Ce^{3+} in YAG:Ce. The assignment of the −15 ppm signal is supported by a linear increase of its integrated intensity with increasing Ce concentration. This has not previously been reported in cerium-substituted YAG. Displacement and broadening of ^{27}Al and ^{89}Y NMR signals due to substitutions of rare-earth ions have been observed in the past in YAG:Tb,[106] $Ln_2Sn_2O_7$ compounds (Ln = lanthanides),[107,108] and $Y_{2-y}Ln_y(Sn,Ti)_2O_7$ compounds.[109] Materials prepared with or without BaF$_2$ and NH$_4$F fluxes yielded nearly identical 1D single-pulse solid-state ^{27}Al MAS NMR spectra, as shown in Supporting Information Figure S4a, indicating that the local environment of Ce is not affected by the use of BaF$_2$ and NH$_4$F flux in the preparation of the YAG:Ce materials. This
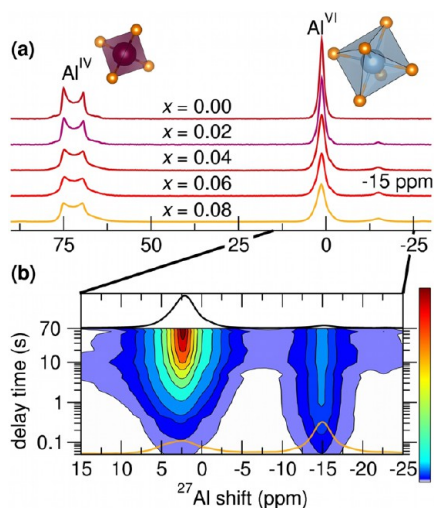
Figure 7. (a) Solid-state single-pulse ^{27}Al NMR spectra (24 kHz MAS) of $Y_{3-x}Ce_xAl_5O_{12}$ acquired at room temperature and 18.8 T with varying amounts of Ce^{3+} in $Y_{3-x}Ce_xAl_5O_{12}$ as indicated. The small signal near −15 ppm is from $^{27}Al^{VI}$ nuclei near substituted Ce^{3+} ions. The spectra with the full spinning sideband manifolds in view are shown in the Supporting Information. (b) Solid-state ^{27}Al NMR saturation recovery plot (14 kHz MAS) of the $^{27}Al^{VI}$ signals of $Y_{2.94}Ce_{0.06}Al_5O_{12}$ at room temperature and 11.7 T, showing the spectra from the shortest and longest delay times at the bottom and top of the plot, respectively. The intensity scale (z axis) is linear.

Figure 8. (a) Cerium composition in $Y_{3-x}Ce_xAl_5O_{12}$ as determined from fits to the solid-state single-pulse ^{27}Al MAS NMR spectra in Figure 7a and b accompanying ^{27}Al linewidths (fwhm) from the same fits. The line in a is the $y = x$ line of Ce composition, x. The error bars, shown for $x = 0.04$, are representative for the other compositions.

observation suggests Ba does not substitute into the lattice in substantial amounts, consistent with the large energy (from DFT calculations) associated with Ba substitution on the Y site of around 5 eV.[110]

The relative population of the $^{27}Al^{VI}$ nuclei corresponding to the −15 ppm signal also amounts to 4 times the Ce concentration in the sample. This is consistent with the first coordination shell of Al^{VI} atoms around Ce, which contains four Al^{VI} atoms with equivalent site symmetries that are equidistant to Ce atoms. Calculation of the Ce concentration from the relative integrated intensities of the −15 ppm signal shown in Figure 8a reveals a linear increase in the amount of $^{27}Al^{VI}$ species in the first-coordination sphere around substituted Ce, which matches the nominal compositions. This indicates that the vast majority of the Ce in the starting materials has been incorporated into the YAG lattice, in agreement with the synchrotron X-ray Rietveld refinement results that showed linear expansion of the unit cell with Ce incorporation. Ce compositions, x, were found from the fits to each ^{27}Al NMR spectrum (example given in Figure 9b) by taking the integrated intensity of the $^{27}Al^{VI}$(1Ce) peak at −15 ppm, dividing by the total intensity of the fitted $^{27}Al^{VI}$ peaks, dividing further by 4 for the number of symmetrically identical $^{27}Al^{VI}$ nuclei in the first-coordination shell around each Ce atom, and finally multiplying by 3 to normalize for the composition ($Y_{3-x}Ce_xAl_5O_{12}$). The displacement of the $^{27}Al^{VI}$ NMR is consistent with the influences of paramagnetic Ce^{3+} species. Therefore, the quantitative results in Figure 8a also demonstrate that the majority of the Ce in the lattice is in the +3 state, corroborating the XANES result. The full-width-at-half-maximum (fwhm) $^{27}Al^{VI}$ linewidths in Figure 8b of the peak near −15 ppm increase linearly with Ce content, indicating increased heterogeneity of the local electronic environments of the $^{27}Al^{VI}$ nuclei nearest Ce with increasing Ce substitution. Finally, since the paramagnetic displacement of
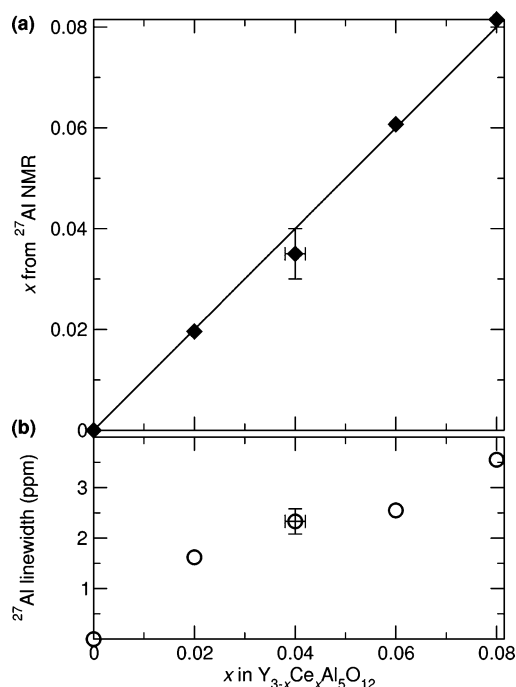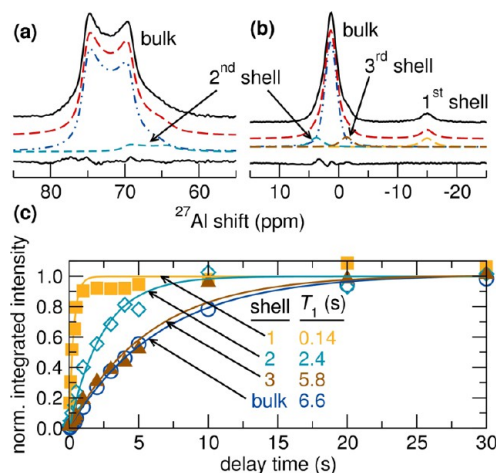

Figure 9. Fits to the (a) Al^{IV} and (b) Al^{VI} components of the 1D solid-state single-pulse ^{27}Al MAS NMR spectra acquired at 24 kHz MAS, room temperature, and 18.8 T for $Y_{2.94}Ce_{0.06}Al_5O_{12}$ based on predicted pseudocontact shift directions from eq 1. The fits have been offset from the data for clarity. (c) Normalized integrated intensities of ^{27}Al signals associated with ^{27}Al nuclei in bulk YAG and in the first-, second-, and third-coordination shells around substituted Ce^{3+} in $Y_{2.94}Ce_{0.06}Al_5O_{12}$ from the saturation-recovery experiment shown in Figure 7b. The solid lines show the exponential fits to the data (integrated intensity = $M_z^0(1 − e^{-t/T_1})$). The T_1 relaxation time decreases with decreasing ^{27}Al−Ce^{3+} distance, indicating increasing ^{27}Al−Ce^{3+} interaction strength with decreasing distance.

the signal from some $^{27}Al^{VI}$ sites near Ce^{3+} is additive with the amount of proximal Ce^{3+} ions, certain ^{27}Al nuclei with two Ce^{3+} ions in the first coordination shell should yield a signal near −30 ppm. Such a signal at −30 ppm is discernible above the noise in the spectrum of the $x = 0.08$ material, though the

relative population of this $^{27}Al^{VI}$ species is very small. Quantification of the ^{27}Al signals from the $x = 0.08$ material established that about 0.44% of Al^{VI} species are near two Ce^{3+} ions, in good agreement with the 0.40% expected in a random distribution of Ce^{3+} in the lattice (assuming effects of Ce^{3+} on nearby ^{27}Al nuclei are additive[109]) and the RMC results.

These results are confirmed by a ^{27}Al NMR spectrum acquired at the very high magnetic field strength of 23.5 T (1 GHz ^1H) in conjunction with 60 kHz MAS. These extraordinary experimental capabilities enable extremely high spectral resolution, as shown in Figure 10 for $Y_{2.91}Ce_{0.09}Al_5O_{12}$.
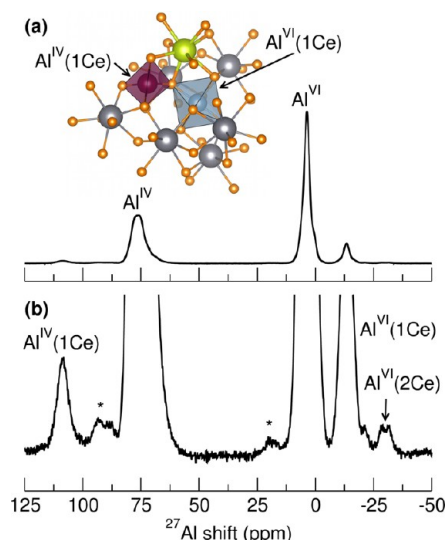
Figure 10. (a) Solid-state single-pulse ^{27}Al MAS NMR spectrum of $Y_{2.91}Ce_{0.09}Al_5O_{12}$ acquired at room temperature, 23.5 T, and 60 kHz MAS with (b) a 40× expansion of the intensity axis. Asterisks indicate small amounts of impurities. The inset depicts the local structures of $Al^{IV}(1Ce)$ and $Al^{VI}(1Ce)$ species near one Ce^{3+} substituent ion (yellow sphere). The spectra with the full spinning sideband manifolds in view is shown in the Supporting Information.

The signal near −15 ppm from $^{27}Al^{VI}$ with one Ce^{3+} ion in its first-coordination shell is still visible, but two peaks near −30 ppm are now visible, due to the higher resolution compared with the spectrum measured at 18.8 T. The ^{27}Al species associated with these latter signals are hypothesized to be due to two distinct local environments of $^{27}Al^{VI}$ nuclei with two Ce^{3+}'s in their first coordination shells. There is also a small shoulder on the low-frequency side of the −15 ppm peak, which may be due to $^{27}Al^{VI}$ nuclei with one Ce^{3+} ion in the first coordination shell and another more distant. These distinct local environments are likely related to the lower-energy Ce sites observed in a previous study[31] and influence the concentration quenching of YAG:Ce. One or more of the distinct sites with a lower energy can lead to quenching by means of energy transfer, provided the two Ce^{3+} ions are within a few tens of Ångstroms from each other. The ratio of relative integrated intensities of the ^{27}Al signals at 3 ppm, −15 ppm, and −30 ppm is 1:0.1402:0.0073, which compares well with the expected ratio of 1:0.1237:0.0029 from a random distribution of Ce^{3+} in YAG:Ce.

Furthermore, the ^{27}Al NMR spectrum acquired at 23.5 T sheds new light on the Al^{IV} species. The $^{27}Al^{IV}$ signals in Figure 10 have considerably smaller linewidths compared with the 18.8 T measurements shown in Figure 7a and no longer have

spinning sidebands in the 100 ppm to 120 ppm region as with the slower spinning speed. Consequently, a signal near 110 ppm is now observed, which is associated with $^{27}Al^{IV}$ atoms with one Ce^{3+} ion in their first-coordination shell. The ratio of relative integrated intensities of the ^{27}Al signals at 75 ppm and 110 ppm is 1:0.0503, close to the expected ratio of 1:0.0619 from a random distribution of Ce^{3+} in YAG. The displaced $^{27}Al^{IV}$ peak at 110 ppm was not observed in the spectrum acquired at 18.8 T, possibly due to nearby spinning sidebands or the broad powder pattern and small population, which could broaden the signal into the baseline at lower magnetic field strengths.

The displacement of $^{27}Al^{VI}$ signals due to proximal Ce^{3+} ions is a result of a short-range through-bond sharing of the Ce^{3+} 4f electron spin density with the surrounding lattice (the Fermi "contact" shift) and a longer-range through-space anisotropic dipolar interaction (also referred to as the "pseudocontact" shift or PCS)[111] between the unpaired Ce^{3+} 4f electron with the ^{27}Al unpaired nuclear spins.[109,112,113] The PCS depends strongly on the internuclear distance between Ce^{3+} and nearby NMR-active nuclei, the crystal-field splitting acting on Ce^{3+}, and the relative orientation of the crystal-field splitting tensor of Ce^{3+} and the vector describing the position of the NMR-active nucleus relative to the Ce^{3+} ion. The expression for the PCS, δ_{pc}, can be expressed as

$$\delta_{pc} = \frac{P}{12\pi r^3}\left[\Delta D_{ax}(3\cos^2(\theta) - 1) + \frac{3}{2}\Delta D_{rh}\sin^2(\theta)\cos(2\phi)\right] \tag{1}$$

where r is the internuclear distance between Ce^{3+} and an NMR-active nucleus, θ and φ are the relative angles of the nucleus position with respect to the D_{zz} and D_{xx} crystal-field splitting components, and $\Delta D_{ax} = D_{zz} - (D_{xx} + D_{yy})/2$ and $\Delta D_{rh} = D_{xx} - D_{yy}$ are the axial and rhombic anisotropies of the crystal-field splitting tensor. The factor P contains the temperature (T) and Ce^{3+} unpaired electron's total angular momentum (J) dependence:

$$P = -\frac{\mu_0\mu_B^2 g_J^2 J(J + 1)(2J - 1)(2J + 3)}{30(kT)^2} \tag{2}$$

Various experimental and calculated values of the crystal-field splitting tensor parameters for YAG:Ce are available in the literature, for example one from Morrison et al.[114] and another from Tanner et al.[115] Both sets yield similar results for the predicted direction and relative magnitudes of the PCS for Al^{IV} and Al^{VI} ^{27}Al nuclei but give different PCS directions for the first ^{89}Y shell around Ce^{3+}. A detailed derivation and explanation of the above equations are provided in the SI, along with depictions of the isosurfaces of the PCS in the YAG structure.

The positions of NMR signals associated with the ^{27}Al species with Ce^{3+} in the first-, second-, and third-coordination shells can be predicted from the calculated PCS, enabling deconvolution of the ^{27}Al NMR spectra. Figure 9a,b shows the excellent fits to the single-pulse ^{27}Al MAS NMR spectra acquired at 18.8 T, which were obtained by using the predicted displacement directions for $Y_{2.94}Ce_{0.06}Al_5O_{12}$ from eq 1; similar results are obtained for the other single-pulse ^{27}Al MAS spectra.[116] The PCS calculated from eq 1 is typically not enough to account for the spectral position of ^{27}Al near Ce^{3+},

indicating a large contribution from the Fermi contact shift. The ^{27}Al signal intensity in Figure 9a is well described by two overlapping second-order quadrupolar lineshapes that are associated with $^{27}Al^{VI}$ species in bulk YAG and second-shell YAG:Ce environments. The calculated relative population of around 7.4% of the $^{27}Al^{VI}$ species with one Ce^{3+} ion in the second-coordination shell agrees well with the expected population of 8% of this $^{27}Al^{VI}$ species expected from a random distribution of Ce^{3+} in $Y_{2.94}Ce_{0.06}Al_5O_{12}$. The $^{27}Al^{VI}$ region, shown in Figure 9b, can be fit well with four peaks with positions at 1.3 ppm, −15 ppm, 3.8 ppm, and −1.3 ppm corresponding to the bulk, first-, second-, and third-coordination shells, respectively. Integration of the signals at 1.3 ppm (bulk), −15 ppm (first-shell from Ce^{3+}), 3.2 ppm (second-shell), and −1.3 ppm (third-shell) yields relative populations of 75.3:8.6:8.1:8.0 for the different $^{27}Al^{VI}$ species, corresponding well with the expected values of 76:8:8:8 for a random distribution of Ce^{3+} in YAG:Ce. These paramagnetically displaced signals have linewidths that are about 10% to 20% broader than the bulk signal. The broadening of the $^{27}Al^{VI}$ signals is likely primarily due to the effect of paramagnetic Ce^{3+} on the surrounding nuclei[117] but may also be due to an inhomogeneous distribution of ^{27}Al environments near Ce^{3+}. The relatively narrow linewidths indicate a high degree of order and little distortion of the local environment of $^{27}Al^{VI}$ nuclei near substituted Ce^{3+}. This supports the Rietveld analyses that show a high degree of crystalline order of the YAG:Ce materials from small atomic displacement parameters and the EXAFS results showing small mean-squared relative displacement factors of Al atoms near the Ce^{3+} substituent ions in YAG:Ce.

Quantification of the $^{27}Al^{VI}$ NMR signals offers support for a random distribution of Ce ions in the +3 state in the YAG lattice in addition to the multicomponent fits in Figure 9a,b. These results are further supported by analyses of the nuclear spin−lattice relaxation times (T_1) of ^{27}Al nuclei in YAG:Ce. Specifically, ^{27}Al nuclei near substituted Ce^{3+} are expected to relax much faster than ^{27}Al nuclei in bulk YAG, due to interactions between paramagnetic Ce^{3+} and nearby ^{27}Al nuclei.[109] Signals from faster relaxing nuclear spins can be enhanced relative to the ^{27}Al signal from bulk YAG by using a saturation-recovery experiment, as shown in Figure 7b for $^{27}Al^{VI}$ species in $Y_{2.94}Ce_{0.06}Al_5O_{12}$. The paramagnetically displaced $^{27}Al^{VI}$ signal near −15 ppm has a significantly shorter T_1 and recovers its equilibrium magnetization much faster than the other $^{27}Al^{VI}$ signals near 1 ppm, consistent with the former ^{27}Al species being nearer to Ce^{3+} substituent ions in the YAG:Ce structure. Integrated areas from fits to each spectrum result in the build-up curves shown in Figure 9c, from which T_1 relaxation times can be extracted by fitting the curves of integrated intensity as monoexponential functions of time.[118] From Figure 9c, it can be seen that the T_1 relaxation time decreases with increasing distance from Ce^{3+} in the YAG structure, with T_1 times of 0.14 s (first-shell), 2.4 s (second-shell), 5.8 s (third-shell), and 6.6 s (bulk). This sequence corroborates weaker interactions between ^{27}Al and Ce^{3+} substituents as the ^{27}Al–Ce^{3+} distances increase and supports the fit to the $^{27}Al^{VI}$ region of the spectra in Figure 9a. The Al^{IV} region from 50 ppm to 125 ppm in Figure 10 shows a similar trend, with a T_1 of 1.9 s associated with $^{27}Al^{IV}$ in bulk YAG (75 ppm), and 50 ms for $^{27}Al^{IV}$ with one Ce^{3+} ion in the first-coordination shell (110 ppm). The T_1 times for the bulk ^{27}Al signals in highly crystalline YAG lattices are relatively long for quadrupolar nuclei. This is related to the purity of the materials,

as well as to the rigidity of the YAG lattice, which is also reflected in the high Debye temperature, Θ_D, as determined from analyses of scattering and EXAFS data.

The paramagnetic effects of Ce^{3+} substituent ions in $Y_{3−x}Ce_xAl_5O_{12}$ also displace the ^{89}Y NMR signals of yttrium atoms in YAG:Ce materials. For example, Figure 11 displays
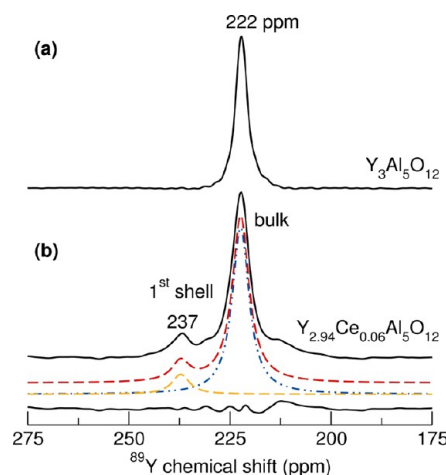

Figure 11. Solid-state single-pulse ^{89}Y NMR spectra (6 kHz MAS) of $Y_{3−x}Ce_xAl_5O_{12}$ with (a) $x = 0$ and (b) 0.06 acquired at room temperature and 19.6 T. (b) Fits to the ^{89}Y signals for $x = 0.06$ Ce^{3+}-substituted YAG, with the difference between the fit and the data shown below the spectrum. The fits have been offset from the data for clarity.

solid-state single-pulse ^{89}Y MAS NMR spectra for bulk unsubstituted YAG and for $Y_{2.94}Ce_{0.06}Al_5O_{12}$. The ^{89}Y MAS NMR spectrum of bulk YAG shown in Figure 11a exhibits a single signal at 222 ppm, which agrees well with previous reports.[104,119] Upon Ce^{3+} substitution, a separate signal appears near 237 ppm, the central signal at 222 ppm broadens, and a shoulder appears on both sides of the bulk ^{89}Y signal at 222 ppm. These features represent paramagnetically induced displacements of the bulk ^{89}Y signal by Ce^{3+} ions and are similar to those observed in the ^{27}Al NMR spectra. From integration of the fit of the solid-state ^{89}Y MAS NMR of $Y_{2.94}Ce_{0.06}Al_5O_{12}$ in Figure 11b, the population of ^{89}Y species with one Ce^{3+} substituent ion in the first-coordination sphere (237 ppm) is estimated to be approximately 11%, slightly higher than the expected 8% for a random distribution of Ce^{3+}. This is likely the result of incomplete relaxation of the bulk ^{89}Y species due to its long T_1 relaxation time, which could overestimate the relative populations of quickly relaxing species near paramagnetic Ce^{3+} (237 ppm peak). Using the crystal-field splitting components from Morrison et al.,[114] eq 1 predicts a displacement to lower frequency (negative ppm direction) for the first shell of ^{89}Y nuclei around Ce^{3+}, while the crystal-field splitting components of Tanner et al.[115] predict a displacement to higher frequency (positive ppm direction), which agrees better with the experimental data in Figure 11b. Congruent with the ^{27}Al spectra, the pseudocontact shift from eq 1 is less than the observed displacement of the signal of ^{89}Y nuclei with one Ce^{3+} substituent nearby (237 ppm) from the bulk ^{89}Y signal (222 ppm), suggesting a significant contribution from the Fermi contact shift.

The calculated pseudocontact shift for ^{27}Al and ^{89}Y nuclei with one Ce^{3+} substituent in the first-coordination shell is much less than the observed displacement of the chemical shift,

suggesting the Fermi contact interaction contributes to the spectral position of these nuclei. The contact interaction cannot reliably be calculated at this time for lanthanides, because the electron−nucleus hyperfine coupling constant for Ce^{3+} in YAG:Ce has not been measured. A significant contribution from the contact interaction suggests considerable sharing of the Ce 4f electron spin density to distances of nearly 4 Å in YAG, which is consistent with previous observations of interactions in lanthanide-substituted inorganic materials.[120,121] For example, purely dipolar interactions between paramagnetic lanthanides and ^{19}F were observed in CaF_2 with the next-nearest neighbor pairs at 4.53 Å, while the Fermi contact was found to affect the nearest F at 2.63 Å in addition to the PCS.[120,121] Since the YAG lattice is more covalent than CaF_2 (based on O and F electronegativities), Fermi contacts at larger distances are not surprising. The sharing of electron spin density through bonds in YAG reflects its highly connected and compact structure that is also consistent with the scattering analyses. Such features result in a rigid structure that tightly holds Ce^{3+} atoms in YAG:Ce, consistent with the small atomic displacement parameters from Rietveld analyses and the mean-square relative displacement parameters from the EXAFS analysis. This leads to the large crystal-field splitting of Ce^{3+} in YAG and a high quantum efficiency. The resistance of the YAG lattice to deformation, even with such a large substituent ion as Ce^{3+}, is also reflected in the narrow linewidths (*ca.* 2.5 ppm in the ^{27}Al spectra and 5.4 ppm in the ^{89}Y spectrum) of the paramagnetically displaced peaks.

Monitoring Ce Sites from ESR. While solid-state NMR spectroscopy is a sensitive tool for probing the local environments of the ^{27}Al and ^{89}Y nuclei in $Y_{3-x}Ce_xAl_5O_{12}$, ESR spectroscopy can be used to probe directly the local environments of the Ce^{3+} activator ions through their unpaired electrons. The ESR spectra acquired at 4 K of Ce^{3+} in $Y_{3-x}Ce_xAl_5O_{12}$ (x = 0.02, 0.04, 0.06, 0.08) in Figure 12 show the primary Ce^{3+} signals with g-tensor values of 2.73, 1.86, and 0.908 (from left to right). These values are in good agreement with values previously measured and calculated in the literature,[122,123] and the broad range of g-tensor values indicates a large anisotropy of the electron spin density. It is noteworthy that all of the ESR spectra from YAG:Ce materials with

different Ce concentrations show the same features. Double integration (DI) of the ESR spectra in Figure 12a yields a linear increase in the DI value with Ce content (SI, Figure S12b), suggesting that all Ce is incorporated into the YAG lattice and is reduced to Ce^{3+} during the reaction, corroborating the synchrotron X-ray and ^{27}Al NMR results previously discussed. The linewidths of the main signal in the ESR spectra at B_o = 2480 G varies linearly with Ce concentration (SI, Figure S12a), which indicates the presence of Ce−Ce dipolar couplings.[124] Small satellite signals reside near the main Ce^{3+} signals, which have been previously attributed to Ce^{3+} in slightly distorted (but distinct) lattice sites in both YAG[122] and YAlO3[125] ESR spectra. There appear to be six distinct Ce sites in the YAG:Ce lattice, manifesting six sets of distinct g-tensor values shown in Table 4. The small satellite signals are present near all three

Table 4. Components of the g-Tensor from the Powder ESR Spectra of $Y_{2.94}Ce_{0.06}Al_5O_{12}$ Acquired at 4 K and 9.4 GHz^a

g_x	g_y	g_z
3.03	1.94	0.946
2.88	1.90	0.924
2.73	1.86	0.908
2.69	1.81	0.899
2.55	1.79	0.878
2.52	1.73	0.864

^{a}The rows of g-factor components do not necessarily imply that the each row is from the same Ce site.

major features in the spectra (SI, Figure S13). A simulation using the parameters in Table 4 is shown at the bottom of Figure 12, which adds support to the existence of six distinct Ce sites. The six Ce sites are most apparent in the region spanning 7000 to 8000 G, shown as an expanded view of the ESR spectra of $Y_{2.94}Ce_{0.06}Al_5O_{12}$ in SI Figure S13.

To confirm that the satellite signals were from Ce^{3+} and not another type of paramagnetic species, temperature-dependent ESR spectra were acquired for the $Y_{2.94}Ce_{0.06}Al_5O_{12}$ material. The satellite ESR signals remained present and broadened in a similar manner to the main YAG:Ce signals with increasing temperature, as expected for satellite signals associated with Ce^{3+} in YAG:Ce. The linewidths of the ESR signals were found to follow the Orbach law, and the line width (Γ) of the signal at 2480 G was fitted using the equation $\Gamma = (e^{\Delta/k_BT} - 1)^{-1} + C$.[126,127] From the fit shown in SI Figure S12c, a value of 14 cm^{-1} was obtained, which corresponds to the energy difference between the lowest two $^2F_{5/2}$ levels of Ce^{3+}. This means thermal energy at room temperature is easily able to excite the 4f electron from the lowest $^2F_{5/2}$ level to the next highest $^2F_{5/2}$ level, since kT at room temperature is around 200 cm^{-1}. Since the transition from the second-lowest-energy 4f level to the lowest-energy 5d level is parity forbidden, the absorption of YAG:Ce will be decreased by populating the second-lowest-energy 4f level.

A previous ESR study attributed the satellite peaks to Ce in distorted lattice sites but was unspecific as to the origin of such distortions.[122] A separate study correlating the concentration of Ce in YAG:Ce to material optical properties suggested that some lower-energy Ce^{3+} sites are present in YAG:Ce, which may be due to distorted lattice sites or to neighboring Ce−Ce ions in the structure.[31] For the x = 0.06 material measured here, a random distribution of Ce in the lattice would result in about 8% of neighboring Ce−Ce ions on the crystallographic Y site. A
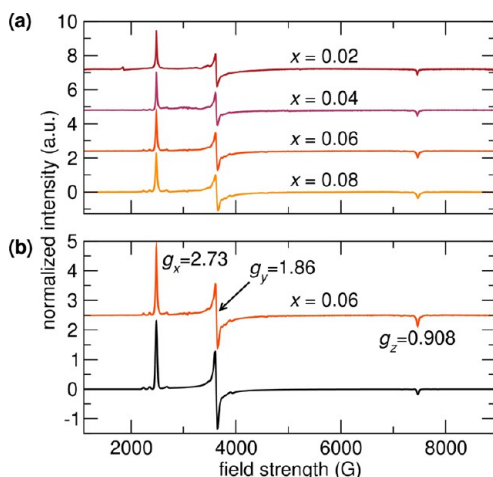

Figure 12. (a) Powder ESR spectra of Ce^{3+} in $Y_{3-x}Ce_xAl_5O_{12}$ acquired at 4 K and 9.4 GHz with compositions as labeled. (b) Amplified experimental spectrum and a simulation of the x = 0.06 material with six different Ce^{3+} sites.

fit to the g_x region (SI, Figure S13) reveals the integrated intensities of the satellite peaks in the ESR spectrum constitutes around 8.8% of Ce ions, in good agreement with a random distribution of Ce in the YAG lattice. This suggests that the satellite peaks and previously observed lower-energy Ce^{3+} sites[31] result from two Ce atoms in neighboring and/or nearby Y sites. This is also consistent with the reverse Monte Carlo simulations of total neutron scattering and high-field solid-state ^{27}Al NMR results, which showed a random distribution of Ce in the YAG:Ce lattice, and multiple local environments of Al near two Ce^{3+} substituents.

CONCLUSIONS

This combined spectroscopic and scattering study has revealed detailed insights about the local environments of Ce^{3+} activator ions in $Y_{3-x}Ce_xAl_5O_{12}$. From high-resolution synchrotron X-ray scattering, we find that the YAG unit cell expands slightly with increasing amounts of Ce (a 0.06% increase in unit cell parameter from $x = 0$ to $x = 0.08$), and this expansion potentially limits the amount of Ce that can be substituted in this crystal using conventional preparative methods. Both X-ray and neutron refinements reveal that the nominal stoichiometries are correct as stated in terms of the refined amounts of Ce on the Y site. An analysis of atomic displacement parameters from X-ray and neutron scattering and mean-square relative displacement parameters from EXAFS suggests a very rigid lattice with a high Debye temperature (θ_D). Few phonon modes would therefore be accessible at room temperature, consistent with the resistance to thermal quenching of luminescence. The observed decrease in θ_D with increasing Ce substitution then provides one reason for the increased quenching of luminescence at high Ce concentrations. This is further supported by neutron PDF analysis, which showed narrow nearest-neighbor peaks corresponding to stiff bonds. Ce L-edge XANES suggests an oxidation state of +3 for Ce in YAG:Ce, corroborated by the solid-state ^{27}Al NMR results. Ce K-edge EXAFS reveals a 3% expansion in the average Ce−O bond distance, compared to the average Y−O distance in the crystal structure. The distortion of the YAG lattice around Ce substitent species decreases with increasing distance from Ce and is no longer observed beyond the fifth-coordination shell (corresponding to a distance of 3.7 Å). High-field solid-state ^{27}Al and ^{89}Y NMR experiments show that the unpaired 4f electron in Ce^{3+} causes a displacement in the NMR signal of nearby nuclei due to paramagnetism, as well as greatly shortened T_1 relaxation times. Correlating the integrated intensities of the ^{27}Al NMR signals with Ce composition shows that the vast majority of the incorporated Ce is paramagnetic Ce^{3+}. Reverse Monte Carlo simulations of total neutron scattering and ^{27}Al NMR spectra are consistent with a random distribution of Ce in the YAG lattice. Finally, ESR spectra of the YAG:Ce phosphor establish that small satellite signals, resulting from neighboring Ce−Ce ions, are present around the main singularities in the amount expected from a random distribution of Ce in the YAG structure.

The results presented here consistently point to some important design rules for effective phosphor materials. The most important, perhaps, is that a rigid host lattice is required, as revealed by the atomic or mean-square relative displacement parameters. This can also be probed *via* the Debye temperature and/or by examining the peak widths of nearest-neighbor peaks in PDFs from total scattering. The rigidity of YAG arises from the highly connected structure and results in a resistance to local bond length and bond angle distortions upon substitution of a large substituent such as Ce^{3+}. The rigidity not only results in high quantum efficiency due to inaccessible phonon modes at operating temperatures but also yields the large crystal-field splitting, provided that the substituent ion is larger than the host lattice ion it replaces. The study points to the importance of a low a concentration of activator ions, in cases such as in YAG:Ce, where the size difference between host site and substituent activator ion is large. A higher concentration of activator ions not only lowers the Debye temperature, making more phonon modes accessible that aid in quenching luminescence, but also introduces greater structural and compositional inhomogeneity. Distorted Ce sites due to neighboring Ce atoms seen at higher concentration potentially provide reduced thermal barriers to nonradiative decay pathways. If the activator ion is substituted for a host site ion of similar size (such as Ce^{3+} substituting for La^{3+}) in a phosphor, larger activator ion concentrations would not be as detrimental to luminescence properties. However, in oxide hosts, this would imply a significantly smaller crystal-field splitting, and hence red-shift of the luminescence, than is seen in YAG:Ce. This study demonstrates the deep understanding that can be obtained on the composition-structure−property relationships of solid-state phosphors, which is expected to aid the development of rational design strategies for syntheses of efficient thermally stable light-emitting compounds with tunable colors. More generally, the synergistic use of state-of-the-art scattering and spectroscopy techniques can be broadly applied to other technologically important classes of heterogeneous functional materials in which the local environments of dopant atoms confer important macroscopic property benefits.

ASSOCIATED CONTENT

Ⓢ Supporting Information
Optical measurements, further synchrotron X-ray and neutron scattering discussion, further NMR discussion, calculation of the pseudocontact shift from lanthanides, Tables S1−S10, and Figures S1−S13 (PDF). This material is available free of charge via the Internet at http://pubs.acs.org.

AUTHOR INFORMATION

Corresponding Authors
*Phone: (805) 893-3673. Fax: (805) 893-4731. E-mail: bradc@engineering.ucsb.edu.
*Phone: (805) 893-6129. Fax: (805) 893-8797. E-mail: seshadri@mrl.ucsb.edu.

Notes
The authors declare no competing financial interest.

ACKNOWLEDGMENTS

3992

dx.doi.org/10.1021/cm401598n | *Chem. Mater.* 2013, 25, 3979−3995

■ REFERENCES

(1) Burroughes, J. H.; Bradley, D. D. C.; Brown, A. R.; Marks, R. N.; Mackay, K.; Friend, R. H.; Burns, P. L.; Holmes, A. B. *Nature* **1990**, *347*, 539−541.

(2) Reineke, S.; Lindner, F.; Schwartz, G.; Seidler, N.; Walzer, K.; Lüssem, B.; Leo, K. *Nature* **2009**, *459*, 234−238.

(3) Nakamura, S. *Science* **1998**, *281*, 956−961.

(4) Schubert, E. F.; Kim, J. K. *Science* **2005**, *308*, 1274−1278.

(5) Pimputkar, S.; Speck, J. S.; DenBaars, S. P.; Nakamura, S. *Nature Photon.* **2009**, *3*, 180−182.

(6) Kim, S.; Kim, T.; Kang, M.; Kwak, S. K.; Yoo, T. W.; Park, L. S.; Yang, I.; Hwang, S.; Lee, J. E.; Kim, S. K.; Kim, S.-W. *J. Am. Chem. Soc.* **2012**, *134*, 3804−3809.

(7) Höppe, H. A. *Angew. Chem., Int. Ed.* **2009**, *48*, 3572−3582.

(8) Ananias, D.; Kostova, M.; Almeida Paz, F. A.; Ferreira, A.; Carlos, L. D.; Klinowski, J.; Rocha, J. *J. Am. Chem. Soc.* **2004**, *126*, 10410−10417.

(9) Duan, C. J.; Wang, X. J.; Otten, W. M.; Delsing, A. C. A.; Zhao, J. T.; Hintzen, H. T. *Chem. Mater.* **2008**, *20*, 1597−1605.

(10) Zeuner, M.; Pagano, S.; Matthes, P.; Bichler, D.; Johrendt, D.; Harmening, T.; Pöttgen, R.; Schnick, W. *J. Am. Chem. Soc.* **2009**, *131*, 11242−11248.

(11) Yeh, C.-W.; Chen, W.-T.; Liu, R.-S.; Hu, S.-F.; Sheu, H.-S.; Chen, J.-M.; Hintzen, H. T. *J. Am. Chem. Soc.* **2012**, *134*, 14108−14117.

(12) Zeuner, M.; Pagano, S.; Schnick, W. *Angew. Chem., Int. Ed.* **2011**, *50*, 7754−7775.

(13) Chen, W.-T.; Sheu, H.-S.; Liu, R.-S.; Attfield, J. P. *J. Am. Chem. Soc.* **2012**, *134*, 8022−8025.

(14) He, J.; Zhao, L.-D.; Zheng, J.-C.; Doak, J. W.; Wu, H.; Wang, H.-Q.; Lee, Y.; Wolverton, C.; Kanatzidis, M. G.; Dravid, V. P. *J. Am. Chem. Soc.* **2013**, *135*, 4624−4627.

(15) Shin, T. H.; Ida, S.; Ishihara, T. *J. Am. Chem. Soc.* **2011**, *133*, 19399−19407.

(16) Buannic, L.; Blanc, F.; Middlemiss, D. S.; Grey, C. P. *J. Am. Chem. Soc.* **2012**, *134*, 14483−14498.

(17) Haase, M.; Schäfer, H. *Angew. Chem., Int. Ed.* **2011**, *50*, 5808−5829.

(18) Wegh, R. T.; Donker, H.; Oskam, K. D.; Meijerink, A. *Science* **1999**, *283*, 663−666.

(19) Bréger, J.; Dupré, N.; Chupas, P. J.; Lee, P. L.; Proffen, T.; Parise, J. B.; Grey, C. P. *J. Am. Chem. Soc.* **2005**, *127*, 7529−7537.

(20) Rawal, A.; Smith, B. J.; Athens, G. L.; Edwards, C. L.; Roberts, L.; Gupta, V.; Chmelka, B. F. *J. Am. Chem. Soc.* **2010**, *132*, 7321−7337.

(21) Riha, S. C.; Parkinson, B. A.; Prieto, A. L. *J. Am. Chem. Soc.* **2009**, *131*, 12054−12055.

(22) Shoemaker, D. P.; Li, J.; Seshadri, R. *J. Am. Chem. Soc.* **2009**, *131*, 11450−11457.

(23) Shayib, R. M.; George, N. C.; Seshadri, R.; Burton, A. W.; Zones, S. I.; Chmelka, B. F. *J. Am. Chem. Soc.* **2011**, *133*, 18728−18741.

(24) Blasse, G.; Bril, A. *Appl. Phys. Lett.* **1967**, *11*, 53.

(25) Nakamura, S.; Mukai, T.; Senoh, M. *Appl. Phys. Lett.* **1994**, *64*, 1687−1689.

(26) Blasse, G. *J. Chem. Phys.* **1967**, *47*, 5139.

(27) George, N. C.; Denault, K. A.; Seshadri, R. *Ann. Rev. Mater. Res.* **2013**, *43*, 2:1−2:21.

(28) Tomiki, T.; Akamine, H.; Gushiken, M.; Kinjoh, Y.; Miyazato, M.; Miyazato, T.; Toyokawa, N.; Hiraoka, M.; Hirata, N.; Ganaha, Y.; Futemma, T. *J. Phys. Soc. Jpn.* **1991**, *60*, 2437−2445.

(29) Ronda, C. R. *Luminescence: From Theory to Applications*; John Wiley & Sons: New York, 2004.

(30) Bachmann, V.; Ronda, C.; Meijerink, A. *Chem. Mater.* **2009**, *21*, 2077−2084.

(31) Setlur, A.; Srivastava, A. *Opt. Mater.* **2007**, *29*, 1647−1652.

(32) Robertson, J. M.; Van Tol, W. H.; Heynen, J. P. H. *Phillips J. Res.* **1981**, *36*, 15−30.

(33) Wu, J. L.; Gundiah, G.; Cheetham, A. *Chem. Phys. Lett.* **2007**, *441*, 250−254.

(34) Pan, Y.; Wang, W.; Liu, G.; Skanthakumar, S.; Rosenberg, R.; Guo, X.; Li, K. K. *J. Alloys Compd.* **2009**, *488*, 638−642.

(35) Furman, J.; Gundiah, G.; Page, K.; Pizarro, N.; Cheetham, A. *Chem. Phys. Lett.* **2008**, *465*, 67−72.

(36) Ghigna, P.; Pin, S.; Ronda, C.; Speghini, A.; Piccinelli, F.; Bettinelli, M. *Opt. Mater.* **2011**, *34*, 19−22.

(37) Gracia, J.; Seijo, L.; Barandiarán, Z.; Curulla, D.; Niemansverdriet, H.; van Gennip, W. *J. Lumin.* **2008**, *128*, 1248−1254.

(38) Muñoz-García, A. B.; Seijo, L. *J. Phys. Chem. A* **2011**, *115*, 815−823.

(39) Wang, J.; Toby, B. H.; Lee, P. L.; Ribaud, L.; Antao, S. M.; Kurtz, C.; Ramanathan, M.; Von Dreele, R. B.; Beno, M. A. *Rev. Sci. Instrum.* **2008**, *79*, 085105−085105−7.

(40) Proffen, T.; Billinge, S. J. L.; Egami, T.; Louca, D. *Z. Kristallogr.* **2003**, *218*, 132−143.

(41) Tucker, M. G.; Dove, M. T.; Keen, D. A. *J. Appl. Crystallogr.* **2001**, *34*, 630−638.

(42) Tucker, M. G.; Keen, D. A.; Evans, J. S. O.; Dove, M. T. *J. Phys.: Condens. Matter* **2007**, *19*, 335215.

(43) Yü, Q. M. *Mater. Sci. Forum* **2010**, *663−665*, 177−182.

(44) Xu, S.; Sun, L.; Zhang, Y.; Ju, H.; Zhao, S.; Deng, D.; Wang, H.; Wang, B. *J. Rare Earth.* **2009**, *27*, 327−329.

(45) Proffen, T.; Egami, T.; Billinge, S. J. L.; Cheetham, A. K.; Louca, D.; Parise, J. B. *Appl. Phys. A: Mater. Sci. Process.* **2002**, *74*, s163−s165.

(46) Bérar, J. F.; Garnier, P. *NIST Spec. Publ.* **1992**, *846*, 212.

(47) Toby, B. H. *J. Appl. Crystallogr.* **2001**, *34*, 210−213.

(48) Momma, K.; Izumi, F. *J. Appl. Crystallogr.* **2011**, *44*, 1272−1276.

(49) Peterson, P. F.; Gutmann, M.; Proffen, T.; Billinge, S. J. L. *J. Appl. Crystallogr.* **2000**, *33*, 1192−1192.

(50) Egami, T.; Billinge, S. J. L. *Underneath the Bragg Peaks: Structural Analysis of Complex Materials*; Elsevier:: Kidlington, Oxford, U. K., 2003.

(51) Farrow, C. L.; Juhas, P.; Liu, J. W.; Bryndin, D.; Božin, E. S.; Bloch, J.; Proffen, T.; Billinge, S. J. L. *J. Phys.: Condens. Matter* **2007**, *19*, 335219.

(52) McGreevy, R. L. *J. Phys.: Condens. Matter* **2001**, *13*, R877.

(53) Tucker, M. G.; Keen, D. A.; Dove, M. T.; Goodwin, A. L.; Hui, Q. *J. Phys.: Condens. Matter* **2007**, *19*, 335218.

(54) Heald, S. M. *Nucl. Instrum. Methods A* **2011**, *649*, 128−130.

(55) Heald, S.; Stern, E.; Brewe, D.; Gordon, R.; Crozier, D.; Jiang, D.; Cross, J. *J. Synchrotron Radiat.* **2001**, *8*, 342−344.

(56) Skanthakumar, S.; Soderholm, L. *Phys. Rev. B* **1996**, *53*, 920−926.

(57) Newville, M. *J. Synchrotron Radiat.* **2001**, *8*, 322−324.

(58) Fenzke, D.; Freude, D.; Fröhlich, T.; Haase, J. *Chem. Phys. Lett.* **1984**, *111*, 171−175.

(59) Woessner, D.; Timken, H. *J. Magn. Reson.* **1990**, *90*, 411−419.

(60) Yesinowski, J. P. *J. Magn. Reson.* **2006**, *180*, 147−161.

(61) Massiot, D.; Fayon, F.; Capron, M.; King, I.; Le Calvé, S.; Alonso, B.; Durand, O. J.; Bujoli, B.; Gan, Z.; Hoatson, G. *Magn. Reson. Chem.* **2002**, *40*, 70−76.

(62) Stoll, S.; Schweiger, A. *J. Magn. Reson.* **2006**, *178*, 42−55.

(63) The BaF$_2$ added as a flux in some samples was not detected in the final products. The absence of BaF$_2$ in the product is because the melting temperature of BaF$_2$ (1560 °C)[128] is near the reaction temperature (1500 °C), enabling vaporization and removal of the BaF$_2$ as the reaction proceeds. Additionally, no Ba substitution in the YAG crystals was detected, because of the size mismatch between Y and the much larger Ba atoms. DFT calculations carried out by Kuklja et al. have suggested that Ba substitution on the Y site has a highly unfavorable energy requirement of around 5 eV.[110]

(64) Vegard, L. *Z. Phys.* **1921**, *5*, 17−26.

(65) Denton, A. R.; Ashcroft, N. W. *Phys. Rev. A* **1991**, *43*, 3161−3164.

(66) Robbins, D. J.; Cockayne, B.; Lent, B.; Duckworth, C. N.; Glasper, J. L. *Phys. Rev. B* **1979**, *19*, 1254−1269.

(67) Tien, T. Y.; Gibbons, E. F.; DeLosh, R. G.; Zacmanidis, P. J.; Smith, D. E.; Stadler, H. L. *J. Electrochem. Soc.* **1973**, *120*, 278−281.

(68) Wynne, R.; Daneu, J. L.; Fan, T. Y. *Appl. Opt.* **1999**, *38*, 3282−3284.

(69) Božin, E. S.; Juhás, P.; Zhou, W.; Stone, M. B.; Abernathy, D. L.; Huq, A.; Billinge, S. J. L. *J. Appl. Crystallogr.* **2009**, *42*, 724−725.

(70) Mellergård, A.; McGreevy, R. L. *Acta Crystallogr., Sect. A* **1999**, *55*, 783−789.

(71) McGreevy, R. L. *Nucl. Intrum. Methods A* **1995**, *354*, 1−16.

(72) Shannon, R. D. *Acta Crystallogr., Sect. A* **1976**, *32*, 751−767.

(73) Brese, N. E.; O'Keeffe, M. *Acta Crystallogr., Sect. B* **1991**, *47*, 192−197.

(74) Trzesowska, A.; Kruszynski, R.; Bartczak, T. J. *Acta Crystallogr., Sect. B* **2004**, *60*, 174−178.

(75) Rack, P. D.; Holloway, P. H. *Mater. Sci. Eng., R* **1998**, *21*, 171−219.

(76) Özen, G.; Demirata, B. *Spectrochim. Acta, Part A* **2000**, *56*, 1795−1800.

(77) Chen, S.-Y.; Lu, Y.-H.; Huang, T.-W.; Yan, D.-C.; Dong, C.-L. *J. Phys. Chem. C* **2010**, *114*, 19576−19581.

(78) Akai, T.; Shigeiwa, M.; Okamoto, K.; Shimomura, Y.; Kijima, N.; Honma, T. *AIP Conf. Proc.* **2007**, *882*, 389.

(79) Edelstein, N. M.; Allen, P. G.; Bucher, J. J.; Shuh, D. K.; Sofield, C. D.; Kaltsoyannis, N.; Maunder, G. H.; Russo, M. R.; Sella, A. *J. Am. Chem. Soc.* **1996**, *118*, 13115−13116.

(80) Kim, Y.-I.; Cadars, S.; Shayib, R.; Proffen, T.; Feigerle, C. S.; Chmelka, B. F.; Seshadri, R. *Phys. Rev. B* **2008**, *78*, 195205.

(81) Dorenbos, P. *J. Lumin.* **2002**, *99*, 283−299.

(82) Zhang, X.; Seo, H. J. *Phys. Status Solidi A* **2010**, *207*, 428−431.

(83) Im, W. B.; George, N.; Kurzman, J.; Brinkley, S.; Mikhailovsky, A.; Hu, J.; Chmelka, B. F.; DenBaars, S. P.; Seshadri, R. *Adv. Mater.* **2011**, *23*, 2300−2305.

(84) Willis, B. T. M.; Pryor, A. W. *Thermal Vibrations in Crystallography*; Cambridge University Press: Cambridge, U. K., 1975.

(85) Cowley, J. M. *Diffaction Physics*; North-Holland Physics Publishing: Amsterdam, 1981.

(86) Diehl, R.; Brandt, G. *Mater. Res. Bull.* **1975**, *10*, 85−90.

(87) Redfern, S. A. T.; Harrison, R. J.; O'Neill, H. S. C.; Wood, D. R. R. *Am. Mineral.* **1999**, *84*, 299−310.

(88) Vasylechko, L.; Senyshyn, A.; Trots, D.; Niewa, R.; Schnelle, W.; Knapp, M. *J. Solid State Chem.* **2007**, *180*, 1277−1290.

(89) Dalba, G.; Fornasini, P. *J. Synchrotron Radiat.* **1997**, *4*, 243−255.

(90) Aggarwal, R. L.; Ripin, D. J.; Ochoa, J. R.; Fan, T. Y. *J. Appl. Phys.* **2005**, *98*, 103514−103514−14.

(91) Pujol, M. C.; Solé, R.; Massons, J.; Gavaldà, J.; Solans, X.; Zaldo, C.; Díaz, F.; Aguiló, M. *J. Appl. Crystallogr.* **2001**, *34*, 1−6.

(92) Dorenbos, P. *J. Phys.: Condens. Matter* **2005**, *17*, 8103−8111.

(93) Yen, W. M.; Shionoya, S.; Yamamoto, H. *Phosphor Handbook*, 2nd ed.; Taylor & Francis Group: London, 2007.

(94) Slack, G. A.; Oliver, D. W.; Chrenko, R. M.; Roberts, S. *Phys. Rev.* **1969**, *177*, 1308−1314.

(95) Hamilton, D. S.; Gayen, S. K.; Pogatshnik, G. J.; Ghen, R. D.; Miniscalco, W. J. *Phys. Rev. B* **1989**, *39*, 8807−8815.

(96) Brgoch, J.; DenBaars, S. P.; Seshadri, R. *J. Phys. Chem. C* **2013**, *117*, 17955−17959.

(97) Grinberg, M.; Sikorska, A.; Kaczmarek, S. *J. Alloys Compd.* **2000**, *300−301*, 158−164.

(98) Pauling, L. *J. Am. Chem. Soc.* **1929**, *51*, 1010−1026.

(99) Runge, V.; Clanton, J.; Lukehart, C.; Partain, C.; James, A. *Am. J. Roentgenol.* **1983**, *141*, 1209−1215.

(100) Bennett, A. E.; Chmelka, B. F.; Eckert, H.; Griffin, R. G.; Vega, S.; Zwanziger, J. W. *Solid-State NMR IV Methods and Applications of Solid-State NMR*, 1st ed.; Springer: New York, 2012.

(101) Brog, K.; Jones, W., Jr.; Verber, C. *Phys. Lett.* **1966**, *20*, 258−260.

(102) Vosegaard, T.; Byriel, I. P.; Pawlak, D. A.; Wozniak, K.; Jakobsen, H. J. *J. Am. Chem. Soc.* **1998**, *120*, 7900−7904.

(103) Massiot, D.; Bessada, C.; Coutures, J. P.; Taulelle, F. *J. Magn. Reson.* **1990**, *90*, 231−242.

(104) Florian, P.; Gervais, M.; Douy, A.; Massiot, D.; Coutures, J.-P. *J. Phys. Chem. B* **2001**, *105*, 379−391.

(105) Lin, Y. S.; Tseng, Y. H.; Liu, R. S.; Chan, J. C. C. *J. Electrochem. Soc.* **2007**, *154*, P16−P19.

(106) Harazono, T.; Yokota, E.; Uchida, H.; Watanabe, T. *Bull. Chem. Soc. Jpn.* **1998**, *71*, 2797−2805.

(107) Cheetham, A. K.; Dobson, C. M.; Grey, C. P.; Jakeman, R. J. B. *Nature* **1987**, *328*, 706−707.

(108) Grey, C. P.; Dobson, C. M.; Cheetham, A. K.; Jakeman, R. J. B. *J. Am. Chem. Soc.* **1989**, *111*, 505−511.

(109) Grey, C. P.; Smith, M. E.; Cheetham, A. K.; Dobson, C. M.; Dupree, R. *J. Am. Chem. Soc.* **1990**, *112*, 4670−4675.

(110) Kuklja, M. M. *J. Phys.: Condens. Matter* **2000**, *12*, 2953−2967.

(111) Bertini, I.; Luchinat, C.; Parigi, G. *Prog. Nucl. Magn. Reson. Spectrosc.* **2002**, *40*, 249−273.

(112) Carrington, A.; McLachlan, A. D. *Introduction to Magnetic Resonance*; Harper and Row: New York, 1967.

(113) Kaupp, M., Bühl, M., Malkin, V. G. *Calculation of NMR and EPR Parameters*, 1st ed.; Wiley-VCH: New York, 2004.

(114) Morrison, C. A.; Wortman, D. E.; Karayianis, N. *J. Phys. C: Solid State Phys.* **1976**, *9*, L191−L194.

(115) Tanner, P. A.; Fu, L.; Ning, L.; Cheng, B.-M.; Brik, M. G. *J. Phys.: Condens. Matter* **2007**, *19*, 216213.

(116) Although the overlap of the satellite transition center bands (*n* = 0 side bands) and the central transition can interfere with the comparison of the integrals for different ^{27}Al sites, the positional difference in ppm from the central transition to the satellite transition center bands is negligible compared with the distance between the separate peaks from distinct ^{27}Al sites. For example, the bulk ^{27}Al^{VI} central transition peak in the spectrum shown in Figure 9b occurs at 1.30 ppm, while the satellite transition center bands occur at 1.18, 1.24, 1.36, and 1.52 ppm.[103] By comparison, the nearest peaks from second- and third-coordination shell ^{27}Al^{VI} sites are displaced by about 2.5 ppm, and the fwhm of these peaks in the fits is around 2.5 ppm. Fits were completed including the satellite transition center bands, and no significant differences in ^{27}Al^{VI} and ^{27}Al^{IV} site populations were found, compared with fits approximating the central transition and satellite center bands for each ^{27}Al site as one summed line shape accounting for their combined contributions to the respective signals.

(117) Van Vleck, J. H. *Phys. Rev.* **1948**, *74*, 1168−1183.

(118) Levitt, M. H. *Spin Dynamics: Basics of Nuclear Magnetic Resonance*, 2nd ed.; Wiley: New York, 2008.

(119) Harazono, T.; Watanabe, T. *Bull. Chem. Soc. Jpn.* **1997**, *70*, 2383−2388.

(120) Bessent, R. G.; Hayes, W. *Proc. R. Soc. London, Ser. A* **1965**, *285*, 430−444.

(121) Baker, J. M.; Hurrell, J. P. *Proc. Phys. Soc.* **1963**, *82*, 742−756.

(122) Baur, J.; Schlotter, P.; Schneider, J. *Adv. Solid State Phys.* **1998**, *37*, 67−78.

(123) Lewis, H. R. *J. Appl. Phys.* **1966**, *37*, 739.

(124) Abragam, A.; Bleaney, B. *Electron Paramagnetic Resonance of Transition Ions*; Clarendon Press: Gloucestershire, U. K., 1970.

(125) Asatryan, H.; Rosa, J.; Mareš, J. *Solid State Commun.* **1997**, *104*, 5−9.

(126) Orbach, R. *Proc. R. Soc. London, Ser. A* **1961**, *264*, 458−484.

(127) Yen, W. M.; Scott, W. C.; Scott, P. L. *Phys. Rev.* **1965**, *137*, A1109−A1112.

(128) Matzke, H. *J. Mater. Sci.* **1970**, *5*, 831−836.